

New particle formation leads to enhanced cloud condensation nuclei concentrations in Antarctic Peninsula

Jiyeon Park¹, Hyojin Kang^{1,2}, Yeontae Gim¹, Eunho Jang^{1,2}, Ki-Tae Park¹, Sangjong Park¹, Chang Hoon Jung³, Darius Ceburnis⁴, Colin O'Dowd⁴, and Young Jun Yoon^{1,*}

¹Korea Polar Research Institute, 26 Songdomirae-ro, Yeonsu-gu, Incheon 21990, South Korea

²University of Science and Technology (UST), 217 Gajeong-ro, Yuseong-gu, Daejeon, Republic of Korea

³Department of Health Management, Kyungin Women's University, Incheon 21041, Republic of Korea

⁴School of Natural Sciences and Centre for Climate and Air Pollution Studies, Ryan Institute, University of Galway, Ireland

*Correspondence to: Y.J. Yoon (yjyoon@kopri.re.kr)

Abstract

Few studies have investigated the impact of new particle formation (NPF) on cloud condensation nuclei (CCN) in remote Antarctica, and none has elucidated the relationship between NPF and CCN production. To address that knowledge gap, we continuously measured the number size distribution of 2.5–300 nm particles and CCN number concentrations at King Sejong Station in the Antarctic Peninsula from January 1 to December 31, 2018. Ninety-seven new particle formation (NPF) events were detected throughout the year. Clear annual and seasonal patterns of NPF were observed: high concentration and frequency of nucleation-mode particles in summer (December–February: 53 NPF cases) and undetected nucleation-mode particles in winter (June–August: no NPF cases). [We estimated the spatial scale of NPF by multiplying the time during which a distinct nucleation mode can be observed at the sampling site by the locally measured wind speed.](#) The estimated median spatial scale of NPF around Antarctic peninsula was found to be approximately 155 km, indicating the large-scale of NPF events. Air back-trajectory analysis revealed that 80 cases of NPF events were associated with air masses originating over the ocean, followed by sea-ice (12 cases), multiple (3 cases), and land (2 cases) regions. We present and discuss three major NPF categories: (1) marine NPF (2) sea-ice NPF, and (3) multiple NPF. Satellite-estimates for sea surface dimethylsulfoniopropionate (DMSP; a precursor of gaseous dimethyl sulfide) data showed

30 that the production of oceanic biogenic precursors could be a key component in marine NPF events,
31 whereas halogen compounds released from ice-covered areas could contribute to sea-ice NPF events.
32 Terrestrial sources (wild life colonies, vegetation, and meltwater ponds) from Antarctica could affect
33 aerosol production in multiple air masses. Out of 97 observed NPF events, 83 cases were characterized
34 by the simultaneous increase in the CCN concentration by 2–270% (median 44%) in the following 1 to
35 36 hours (median 8 hours) after NPF events. Overall, Antarctic NPF events were found to be a significant
36 source of particles with different physical characteristics and related to biogenic sources in and around
37 the Antarctic Peninsula, which subsequently grew to cloud condensation nuclei.

38

39 **1. Introduction**

40 Antarctic peninsula is warming more rapidly than Earth’s global mean rate (Chen et al., 2009;
41 Vaughan et al., 2003), leading to shrinking sea-ice coverage and consequent sea-level rise (Pritchard et
42 al., 2009). In the Antarctic region, ambient aerosols play a crucial role in governing radiative transfer,
43 directly by the scattering and absorption of solar radiation and indirectly by acting as cloud condensation
44 nuclei (CCN) (IPCC, 2013). The magnitude of the radiative forcing caused by the interactions between
45 aerosols and CCN remains highly uncertain due to a poor understanding of pristine natural aerosols
46 (Carslaw et al., 2013). To reduce this uncertainty, the physicochemical properties of aerosol particles (e.g.,
47 number concentrations, size distributions, chemical compositions, and hygroscopicity) have been studied
48 at several Antarctic stations including King Sejong Station (Kim et al., 2019), Aboa (Asmi et al., 2010;
49 Virkkula et al., 2006), Dome C (Järvinen et al., 2013), Halley (Lachlan-Cope et al., 2020; O’Dowd et al.,
50 1997), Kohn (Weller et al., 2018), McMurdo (Giordano et al., 2018; Liu et al., 2018), Neumayer (Teinilä
51 et al., 2014; Weller et al., 2015), Princess Elisabeth (Herenz et al., 2019) and Syowa (Hara et al., 2011;
52 Ito, 1993). Furthermore, open ocean and coastal Antarctic expeditions such as SIPEXII (Sea Ice Physics
53 and Ecosystems eXperiment, 2012; Humphries et al., 2015; Humphries et al., 2016), PEGASO (Plankton-
54 derived Emissions of trace Gases and Aerosols in the Southern Ocean, 2015; Dall’Osto et al., 2017;
55 Decesari et al., 2020; Fossum et al., 2018), ACE-SPACE (Antarctic Circumnavigation Expedition – Study

56 of Preindustrial-like Aerosol Climate Effects, 2017; Schmale et al., 2019; Walton and Thomas, 2018),
57 PCAN (Polar Cell Aerosol Nucleation, 2017; Simmons et al., 2021); PI-ICE (Polar atmosphere-ice-ocean
58 Interactions: Impact on Climate and Ecology, 2019; Brean et al., 2021; Dall'Osto et al., 2022) studies on
59 the influences of marine aerosols on climate and ecology. Overall, aerosol particle number concentrations
60 follow a clear annual trend, being much higher in austral summer than in other seasons (Järvinen et al.,
61 2013; Kerminen et al., 2018; Weller et al., 2011). For instance, Kim et al. (2017) found that summertime
62 concentrations in the Antarctic Peninsula were ~20 times higher than in winter. This pattern can be largely
63 explained by new particle formation (NPF) events.

64 Precursor gases for NPF in this region can originate from the ocean, sea-ice, meltwater ponds,
65 terrestrial animal colonies, anthropogenic activity and continental ecosystem. Oceanic emissions of
66 dimethyl sulfide (DMS) represent the largest natural sulfur source in the Antarctic atmosphere (Simó,
67 2001), and its photooxidation is a key process contributing to NPF (Giordano et al., 2017; Jang et al.,
68 2019 and 2022). For instance, in situ (Saiz-Lopez et al., 2007) and satellite (Schönhardt et al., 2008)
69 measurements have shown Antarctica to be an iodine emission hotspot, particularly from the sea-ice in
70 the Weddell Sea during spring (Atkinson et al., 2012). Indeed, Sipilä et al. (2016) measured iodic acid
71 (HIO_3) in Antarctica and found that the Antarctic oceanic regions may be strong sources of molecular
72 iodine, which is then converted to HIO_3 in gas-phase reactions. Dall'Osto et al. (2017) reported that
73 microbiota in sea-ice were associated with atmospheric organic nitrogen formation in the Southern Ocean
74 near Antarctica. According to Kyrö et al. (2013), the precursor vapors responsible for NPF and subsequent
75 growth could originate from the cyanobacteria, which are abundant in Antarctic meltwater ponds. In
76 addition, continental Antarctica is a habitat for various types of seabirds and penguins, with guano species
77 acting as a crucial source of ammonia and organic compounds and may contribute to NPF in coastal
78 Antarctic areas (Schmale et al., 2013; Weber et al., 1998; Zhu et al., 2011). At continental South Pole NPF
79 event are commonly associated with the local anthropogenic pollution during calm weather conditions
80 (Park et al., 2004). In addition, the biomass burning aerosol from South American continental outflow has
81 been observed at Troll Research Station (Fiebig et al., 2009). During the daytime, higher radiation

82 enhances photo-active emissions from land ecosystems (mosses, grasses, and lichens) of the Antarctic
83 Peninsula and can lead to NPF and aerosol growth (Decesari et al., 2020; Quéléver et al., 2022; Schmale
84 et al., 2013). However, land sources are rather unlikely due to a small footprint of emerging land and the
85 associated short overpass over the sparse vegetation.

86 In recent years, long-term records of aerosol size distribution have become an important aspect of
87 investigations into the sources and dynamical processes of NPF. The majority of Antarctic field studies
88 have focused on the annual and spatial patterns of the number size distribution of particles > 10 nm (Belosi
89 et al., 2012; Järvinen et al., 2013; Kim et al., 2019; Kyrö et al., 2013; Lachlan-Cope et al., 2020). Although
90 NPF events are typically characterized by a rapid increase in the number concentration of cluster from 1–
91 3 nm (Kulmala et al., 2004), datasets for these types of aerosol size distribution remain rare. To date,
92 number size distribution of particles > 3 nm has been reported by Asmi et al. (2010) at Aboa during from
93 December 29, 2006 to January 29, 2007; by Pant et al. (2011) at Maitri from January 1 to February 28,
94 2015; by Weller et al. (2015) at Neumayer from January 20 to March 26, 2012; by Jokinen et al. (2018)
95 at Aboa from November 2014 to February 2015; by Weller et al. (2018) at Kohnen during January 2015
96 and 2016; by Quéléver et al. (2022) at Marambio during the austral summer between January 15 and
97 February 25, 2018; and by Brean et al. (2021) during the PI-ICE cruise from January 25 to February 4,
98 2019. However, all of these measurements were made during the Antarctic summer due to restricted
99 access and, therefore, limited information on seasonal cycles.

100 Newly formed particles can grow into larger sizes that act as CCN, becoming relevant for cloud
101 formation (O’Dowd, 2002; Williamson et al., 2019). In a highly pristine atmosphere such as Antarctica,
102 where CCN concentration is extremely low (Kim et al., 2017), NPF may be a significant phenomenon
103 controlling the CCN budget (Kyrö et al., 2013). For instance, Herenz et al. (2019) showed that an elevated
104 $CN_{2.5}$ (total number concentration of particles > 2.5 nm) during NPF events was accompanied by an
105 increase in CCN concentrations at Princess Elisabeth during austral summer (December to February,
106 2013–2016). Ship-based observations during the ACE-SPACE found that the fraction of particle serving
107 as CCN was higher near the coast of Antarctica compared to open ocean, resulting from multiple

108 processing cycles of dissipating and condensing clouds and/or the higher availability condensable gases
109 originating from marine microbial activity (Schmale et al., 2019). In addition, seasonal variability in
110 $CN_{2.5-10}$ (number concentration of particles within the 2.5 nm and 10 nm range and attributed to NPF)
111 and CCN concentrations at King Sejong Station from March 2009 to December 2016 were investigated
112 by Kim et al. (2019), who concluded that CCN concentrations during NPF events increased by ~11%
113 compared to the background concentration. However, to date, only one study (Kim et al., 2019) has
114 reported the contribution of NPF to CCN in the Antarctic Peninsula, and that study did not consider
115 aerosol number size distribution.

116 In this study, we continuously recorded the number size distribution of 2.5–300 nm particles and
117 CCN number concentrations at King Sejong Station in the Antarctic Peninsula from January 1, 2018, to
118 December 31, 2018. Our primary goals were to (1) characterize the seasonal variation and occurrence of
119 NPF events from the perspective of aerosol physical properties (total number concentration, number size
120 distribution, formation and growth rates, and condensation sink); (2) improve our understanding of the
121 major sources (including open ocean, sea-ice, and land) and processes influencing NPF and particle
122 growth; and (3) estimate the contribution of atmospheric NPF to CCN activity in this pristine environment.
123 To our knowledge, this is the first study to present direct evidence of CCN production associated with
124 NPF and growth events in the Antarctic Peninsula, using simultaneous measurements of particle number
125 size distributions (down to 3 nm) and CCN properties for a full year.

126

127 **2. Experimental methods**

128 **2.1. Sampling site and instrumentation**

129 Continuous measurements of the physical properties of aerosol particles were conducted from
130 January 2018 to December 2018 at King Sejong Station in the Antarctic Peninsula (62.22° S, 58.78° W).
131 Full details of the sampling site and measurement setup are given in Kim et al. (2017). In brief, a
132 cylindrical stainless inlet (0.1 m diameter and 5.2 m length; total flow rate of the sampled air was 150 L
133 min^{-1}) was placed on the observatory roof following Global Atmosphere Watch aerosol measurement

134 guidelines and recommendations. Two condensation particle counters (TSI model 3776 CPC and TSI
135 model 3772 CPC) were used to measure the total number concentration of particles larger than 2.5
136 (corresponding data $CN_{2.5}$) and 10 nm (corresponding data CN_{10}) every 1 s, respectively. The aerosol
137 sample flow rates of TSI model 3776 CPC and TSI model 3772 CPC were 1.5 and 1.0 L min⁻¹, respectively.
138 A nano-scanning mobility particle sizer (nano-SMPS) consisting of a nano-differential mobility analyzer
139 (nano-DMA) (TSI model 3085, USA) and an ultrafine condensation particle counter (TSI model 3776,
140 USA) was used to measure the number size distribution of particles from 2.5–64 nm every 3 minutes. The
141 aerosol flow rate was 1.5 L min⁻¹ and the sheath flow rate was 15 L min⁻¹ inside the nano-DMA.

142 The particle number size distribution (from 10–300 nm every 3 min) was measured with a standard-
143 SMPS consisting of a long DMA (TSI model 3081, USA) and a CPC (TSI model 3772, USA). The aerosol
144 flow rate was 1.0 L min⁻¹, and the sheath flow rate was 10 L min⁻¹ inside the long DMA. To obtain the
145 number size distribution of particles from 2.5–300 nm, the nano-SMPS and standard-SMPS were merged.
146 For particle diameters 2.5–20 nm, nano-SMPS data were chosen because this was optimized to operate
147 with a smaller particle diameter. In the nano-DMA, the aerosol residence time can be reduced by
148 shortening the inlet transport passage (5.0 cm) and increasing the inlet flow (up to 16.5 L min⁻¹) (< 10 nm)
149 (Chen et al., 1998). Hence, the number size distribution data from both nano-SMPS and standard-SMPS
150 were merged at a diameter of 20 nm. Furthermore, three-point median filter and five point moving average
151 were performed on merging the number size distribution data to remove nano-SMPS noise, as suggested
152 by Kulmala et al. (2012).

153 The black carbon (BC) concentration was measured using an aethalometer (AE22, Magee Scientific
154 Co., USA) every 5 min to examine long-range polluted aerosol transport from other continents and to
155 assess the influence of local pollution from the station. The flow rate through a sharp-cut 2.5 µm cyclone
156 (BGI, Inc., USA) was set to 5 L min⁻¹. The CCN counter (CCNC: CCN-100, Droplet Measurement
157 Technologies, USA) measured CCN number concentrations at five different supersaturation levels of 0.2%
158 0.4%, 0.6%, 0.8%, and 1% every 30 minute. The total flow rate in the CCN counter was 0.5 L min⁻¹. The
159 sample and sheath flow rates of the CCN counter were 0.05 and 0.45 L min⁻¹, respectively. In addition,

160 basic meteorological parameters (temperature, pressure, relative humidity (RH), wind speed, wind
161 direction, and solar radiation intensity) were measured using an automatic weather station (Vaisala
162 HMP45).

163

164 **2.2. Data evaluation**

165 As the observatory is located ~400 m southwest of the main station buildings and several kilometers
166 away from other research stations, measurement data were impacted by local emissions from station
167 activities (e.g., power generators and incineration) or anthropogenic pollutions near the observatory (e.g.,
168 plumes from other research station about several kilometers, vessels providing research station supply,
169 and commercial cruise vessels). To obtain an unperturbed aerosol population of pristine Antarctic
170 environment, contaminated measurements were removed manually based on wind direction, wind speed,
171 BC concentration, and total particle number concentration. The following data elimination procedure was
172 applied: (1) the measurements taken within wind sector of 355° and 55° were discarded as directly
173 impacted by local pollution sources; (2) relative wind speed below 2.0 m s^{-1} , as stagnant conditions would
174 have facilitated contaminated particle propagation to the measurement location; (3) equivalent BC mass
175 concentrations exceeding 50 ng m^{-3} , because elevated BC concentration unambiguously pointed at
176 polluted particles; and (4) a sharp increase in the total number concentration over the entire particle
177 diameter range in a short time scale of less than an hour, as such abrupt peaks and spikes are related to
178 potential contamination or instrumental malfunctions. For instance, CPC and SMPS data were removed
179 for time periods when particle number concentrations suddenly increased to more than twice the
180 background values.

181 Based on a four-year (2016-2019) BC dataset, six types of Antarctic Peninsula air-pollution levels
182 were identified (Grigas et al., 2017): (1) pristine air with BC concentrations $< 15 \text{ ng m}^{-3}$, (2) clean air with
183 BC levels $15\text{--}50 \text{ ng m}^{-3}$, (3) slightly polluted air with BC levels $50\text{--}100 \text{ ng m}^{-3}$, (4) moderately polluted
184 air with BC levels $100\text{--}300 \text{ ng m}^{-3}$, (5) polluted air with BC levels $300\text{--}1000 \text{ ng m}^{-3}$, and (6) extremely
185 polluted air with BC concentrations $> 1000 \text{ ng m}^{-3}$ (Figure 1). Previously, BC data were used as indicators

186 for local contamination in Antarctica when BC concentration level exceeded 50 ng m^{-3} (Herenz et al.,
187 2019) or 100 ng m^{-3} (Jang et al., 2018; Kim et al., 2017; Kim et al., 2019; Weller et al., 2011; Weller et
188 al., 2015). Hara et al. (2019) measured BC concentration at Syowa station Antarctica from February 2005
189 until December 2016. They found that the daily median BC concentrations were below the detection limit
190 (0.2 ng m^{-3}) to 63.8 ng m^{-3} at Syowa Station (median, 1.8 ng m^{-3} ; mean, 2.7 ng m^{-3} during the measurement
191 period). During the ACE-SPACE expedition, BC concentration reach its background levels of 19.2 ng m^{-3}
192 (3 ng m^{-3}) (Schmale et al., 2019). Arctic shipborne-observations measured BC concentration throughout the Arctic
193 Ocean and Pacific Ocean during the summer of 2017, all pointing to pristine clean marine air masses with
194 BC values of approximately $20 \pm 10 \text{ ng m}^{-3}$. (Park et al., 2020).

195 Of the total time period assessed, pristine air conditions represented 30% (mean value of BC: 6 ± 6
196 ng m^{-3}), clean for 44% (mean value of BC: $30 \pm 10 \text{ ng m}^{-3}$), lightly polluted 19% (mean value of BC: 69
197 $\pm 14 \text{ ng m}^{-3}$), moderately polluted 6% (mean value of BC: $150 \pm 47 \text{ ng m}^{-3}$), polluted 1% (mean value of
198 BC: $499 \pm 174 \text{ ng m}^{-3}$), and extremely polluted less than 1% (mean value of BC: $1537 \pm 595 \text{ ng m}^{-3}$).
199 Together, pristine and clean air conditions accounted for $\sim 74\%$ of the time with the remaining 26% (BC
200 $> 50 \text{ ng m}^{-3}$) removed prior to data analysis.

201

202 **2.3. Definition of NPF and growth events**

203 NPF events were visually identified by the particle number size distribution based on the protocol
204 described by Dal Maso et al. (2005) and Kulmala et al. (2012). Here, these were defined when a distinct
205 new mode of particles (initially $< 25 \text{ nm}$), appearing in the particle number size distribution at nucleation-
206 mode size ($3\text{--}25 \text{ nm}$), prevailed for more than an hour. Using these criteria, the particle size distribution
207 data showed that in some cases, there was only a short burst of nucleation-mode particles without clearly
208 discernible particle growth, whereas in other cases, particle formation with subsequent particle growth
209 lasted for several hours, representing a regional-scale phenomenon (Ström et al., 2009). This enabled us
210 to determine the particle growth rate (GR), which is not possible during short bursts of nucleation-mode
211 particles.

212 The particle growth and formation rates along with the condensation sink were calculated from the
213 measured particle number size distribution. The GR was determined using the maximum concentration
214 and mode-fitting methods (Dal Maso et al., 2005; Yli-Juuti et al., 2009). GR was calculated by a linear fit
215 through the geometric mean diameter of the nucleation-mode particles as a function of time during NPF.
216 The formation rate (FR) of nucleation-mode particles (J_{3-25}) was calculated by taking into account the
217 time evolution of the particle number concentration in this size range and particle losses due to the
218 coagulation sink and condensational growth out of the size range (Kulmala et al., 2012). The surface area
219 of particles available for the condensation of gaseous molecules can be characterized by a condensation
220 sink (CS), which determines how rapidly vapor molecules condense onto pre-existing particles (Collins
221 et al., 2017; Dal Maso et al., 2002).

222

223 **2.4. Backward trajectory analysis and potential source regions**

224 Air mass back trajectories were obtained using the Hybrid Single-Particle Lagrangian Integrated
225 Trajectory (HYSPLIT) model to investigate their relationships with the physical characteristics of aerosol
226 particles (Draxler and Hess, 1998). The 2 days air mass back trajectories (48 hours) were determined at
227 hourly intervals and combined with satellite-derived geographical information to estimate the transport
228 history of the air masses arriving at the observation site (Jang et al., 2022 and Park et al., 2021). The
229 potential origins of the aerosols were divided into three categories based on the retention time of the 2
230 days back trajectories over three major domains: ocean (including the Weddell and Bellingshausen Seas),
231 sea-ice, and land (including the Antarctic Peninsula). Daily geographical information on ocean, sea-ice,
232 and land area was obtained from the Sea Ice Index (25 km resolution) provided by the National Snow and
233 Ice Data Center (NSIDC). The sea-ice zone was defined as the area with a sea-ice coverage >15% (Stroeve
234 et al., 2016). Air masses that passed over the Weddell and Bellingshausen Sea-regions were categorized
235 as originating from the ocean (i.e. > 50% retention over the ocean region). The air masses that frequently
236 advected over the sea-ice region were categorized as originated over the sea-ice (i.e. > 50% retention over
237 the sea-ice domain). Air masses that traveled through the Antarctic Peninsula were categorized as

238 originating from the land (i.e. > 50% retention over the land). Finally, the air masses which passed over
239 the ocean, sea-ice, and land regions simultaneously were categorized as originating from the multiple
240 regions (i.e., 20–40 % retention over each ocean, sea-ice, and land domain).

241 To evaluate the influence of oceanic biological characteristics on NPF properties, the phytoplankton
242 biomass of the ocean domains was estimated by calculating their chlorophyll concentration from the
243 Moderate Resolution Imaging Spectroradiometer on the Aqua (MODIS-Aqua) satellite at 4 km resolution
244 during the entire study period. Phytoplankton produces dimethylsulfoniopropionate (DMSP, a precursor
245 of gaseous DMS) and other organic vapors all of which are potential precursors to new particle formation.
246 Thus, the spatiotemporal distribution of sea-surface DMSP could be an indicator of contemporary DMS
247 emissions. The total DMSP concentration on the sea-surface was estimated using the algorithm developed
248 by Galí et al. (2015). The algorithm for the total DMSP concentration was based on the satellite-derived
249 chlorophyll concentration and photosynthetic radiation exposure. To calculate the air mass exposures to
250 ocean chlorophyll and DMSP (Jang et al., 2019), hourly back trajectory position was combined with
251 satellite-derived chlorophyll concentration and total DMSP concentration, providing a good measure for
252 quantitatively investigating the biological exposure history of sampled air over the several days before its
253 arrival at the observation site (Park et al., 2018 and 2021). However, satellites are not typically used to
254 directly measure the biomass of sea ice algae because satellite sensors cannot penetrate through thick
255 layers of sea ice to directly measure the biomass of algae beneath it (Lee et al., 2015; Lange et al., 2017).
256 Thus, calculated chlorophyll exposures (i.e., satellite-estimates of biological activity) cannot account for
257 the biological activities thriving within and beneath of the sea ice.

258

259 **3. Results and discussion**

260 **3.1. General features and annual cycle**

261 We investigated the overall seasonality of particle number size distributions focusing on NPF events.
262 In addition, local meteorological parameters (e.g., temperature, RH, wind speed, wind direction, pressure,
263 and solar radiation) and air mass back trajectories were used to support the interpretation of the seasonal

264 trends of the particle number size distribution and the dynamics of NPF events observed at the station.

265 **3.1.1. Particle number concentrations and size distributions**

266 Figure 2 shows a time series of the one-hour average total particle number concentration and size-
267 segregated particle number concentrations over the entire measurement period conforming to pristine (BC
268 $< 15 \text{ ng m}^{-3}$) and clean (BC: $15\text{--}50 \text{ ng m}^{-3}$) conditions. In addition, monthly medians for total number
269 concentration of particles, size-segregated particles number concentration, CCN number concentration at
270 supersaturation of 0.4%, and meteorological parameters are included in Table 1. The $\text{CN}_{2.5}$ and CN_{10}
271 ranged from 60 to 3982 cm^{-3} and 30 to 3304 cm^{-3} , respectively. The annual median number concentrations
272 of particles for the nucleation mode (N_{NUC} ; 2.5–25 nm in diameter), Aitken mode (N_{AIT} ; 25–100 nm in
273 diameter), and accumulation mode (N_{ACC} ; 100–300 nm in diameter) were 46.8 cm^{-3} , 53.5 cm^{-3} , and 21.7
274 cm^{-3} , respectively. The highest median N_{NUC} , N_{AIT} , and N_{ACC} values were recorded in December (193.5
275 cm^{-3}), December (227.6 cm^{-3}), and January (83.8 cm^{-3}), respectively (Table 1). The lowest N_{NUC} , N_{AIT} ,
276 and N_{ACC} values were recorded during austral winter in June – 12.2 cm^{-3} , 12.5 cm^{-3} and 9.2 cm^{-3} ,
277 respectively. Overall, clear annual and seasonal patterns of particle number concentrations in all size
278 classes were observed: high concentrations in summer (December–February) and low concentrations in
279 winter (June–August), similar to those observed at Marambio Station in the Antarctic Peninsula (Asmi et
280 al, 2018), at coastal Neumayer Station (Weller et al., 2011), at Concordia Station Dome C (Järvinen et al.,
281 2013), and at Troll Station (Fiebig et al., 2014). Furthermore, the hourly average CN_{10} value was
282 positively correlated with the hourly average N_{NUC} ($R = 0.88$; not shown), implying that the summer
283 maximum of total particle number concentrations was largely influenced by newly formed particles in the
284 Antarctic atmosphere.

285 **3.1.2. Influence of meteorological parameters on NPF events**

286 The meteorological parameters after data filtering (BC $< 50 \text{ ng m}^{-3}$ indicating pristine and clean
287 conditions) were characterized by a solar radiation range of 0–919 W m^{-2} (median 10.7 W m^{-2}), a
288 temperature range of $-20\text{--}6 \text{ }^{\circ}\text{C}$ (median $-1.2 \text{ }^{\circ}\text{C}$), an RH range of 52–98 % (median 88 %), a pressure
289 range of 950–1022 hPa (median 988 hPa), a wind speed range of 0.3–21 m s^{-1} (median 7.4 m s^{-1}), and

290 wind direction range of 3–357° (median 296°) (Figure S1). To understand impacts on the particle number
291 size distributions, we determined the relationships between the size-segregated particle number
292 concentrations and meteorological parameters (Figure S2). CN_{10} , N_{NUC} , N_{AIT} , and N_{ACC} were positively
293 correlated with both solar radiation intensity and temperature. In particular, N_{NUC} had the highest
294 correlation with solar radiation intensity ($R = 0.39$) of any meteorological condition, suggesting that solar
295 radiation is one of the most important factors influencing NPF events, as it can drive photochemical
296 reactions leading to the production and further reaction of precursor gases. In contrast, there was a weak
297 anticorrelation between RH and N_{NUC} , supporting the view that NPF occurs preferentially at low RH
298 (Dada et al., 2017; Hamed et al., 2011; Jeong et al., 2010; Laaksonen et al., 2008). Field observations
299 have reported that during NPF events, RH was negatively related to the number concentration of freshly
300 formed particles (Jeong et al., 2004; Lachlan-Cope et al., 2020; Weber et al., 1997) because of the
301 enhanced coagulation from scavenging effect of sub-3 nm nanoparticles at high RH and the diminished
302 solar radiation at high RH. Previously, some NPF events were associated with high wind speeds at various
303 Antarctic stations, such as Neumayer (Weller et al., 2015) and Aboa (Asmi et al., 2010; Virkkula et al.,
304 2007). These studies found an enhanced particle number concentration < 10 nm during stormy weather
305 and suggested ion production by frictional processes in fast-moving snow and ice crystals, followed by
306 subsequent ion-mediated nucleation during strong winds. However, in our study, wind speed was not
307 correlated with N_{NUC} ($R = -0.18$), N_{AIT} ($R = -0.04$), or N_{ACC} ($R = -0.05$), as recently suggested by Liu et
308 al. (2018). Our results indicated that wind speed did not affect NPF events. A possible explanation for the
309 wind speed independence is that an increase in wind speed contributes to the increase of cluster size ion
310 number concentrations by friction processes (Virkkula et al., 2007), but it was also accompanied by
311 cloudy conditions. In summary, the elevated N_{NUC} values (i.e., indicator of NPF events) at King Sejong
312 Station were more likely to be accompanied by high solar radiation, high temperature, and low RH,
313 regardless of wind speed. Recent studies concluded that Antarctic NPF occurred under combined high
314 solar radiation, high temperature and low RH conditions, similar to previous study measured at the
315 Marambio Antarctic research station (Quéléver et al., 2022). Quéléver et al. (2022) found all NPF events

316 were observed during the daytime with high solar radiation (clear-sky conditions), mostly with above-
317 freezing temperature and with low RH.

318 **3.1.3. Characteristics of NPF events**

319 NPF events in this study were identified based on the size distribution data measured using the
320 standard-SMPS (Figure 2e) and nano-SMPS (Figure 2f). During the pristine and clean periods
321 (comprising of 355 observation days and 169166 size distribution spectra for the standard-SMPS, and of
322 349 observation days and 165259 size distribution spectra for nano-SMPS), NPF events were frequently
323 observed at King Sejong Station, as shown by the size distribution data (Figure 2f). 97 events (26% of
324 observation days) with elevated N_{NUC} were observed when taking place in pristine ($\text{BC} < 15 \text{ ng m}^{-3}$) and
325 clean ($\text{BC}: 15\text{--}50 \text{ ng m}^{-3}$) conditions. Median value of BC concentrations during NPF events was 21.0 ng
326 m^{-3} , similar to that of whole measurement periods after data filtering (median BC value: 18.8 ng m^{-3})
327 (section 2.2). This indicated that NPF events are independent of occasional increases of BC during clean
328 periods. The NPF events were classified into: (1) burst event and (2) nucleation with growth event
329 according to the classification by Dal Maso et al. (2005) as seen in Figure S3. The burst events and
330 nucleation with growth events were observed on 1 January 2018 and 16 December 2018, respectively.
331 NPF events were more frequently observed in summer (~55%) than in any other season (Figure 4), with
332 the highest frequency in January (22%) and December (22%) followed by spring (September–November,
333 34%) and autumn (March–May, 11%). Similar results were reported by Järvinen et al. (2013) based on
334 observations from Dome C and Kim et al. (2019) based on observations from King Sejong Station.
335 Although Järvinen et al. (2013) reported winter events that occurred in the absence of sunlight, we did
336 not detect NPF events during austral winter from May through to August.

337 In order to investigate the seasonal characteristics of NPF event, we compared mean size
338 distributions of aerosol particles for summer, spring (transition period of the melting ocean), and autumn
339 (transition period of refreezing of the ocean) (Figure S4). Trimodal distributions were presented in all
340 seasons excepting winter when nucleation mode or particle formation was not observed. For instance, a
341 trimodal distribution was seen at 7 nm, 30 nm, 122 nm during summer months. The number concentration

342 of nucleation and Aitken modes were higher than the accumulation modes, indicating that NPF event
343 regulates the aerosol processes in Antarctic peninsula. The largest mode at 126 nm or 103 nm may be due
344 to a combination of primary (produced by bubble-bursting process) and secondary (produced by gas-to-
345 particle conversion process) aerosol components. Results are broadly in line with previous results
346 published from the Arctic and Antarctic regions. A ship-borne field campaign over Arctic Ocean found a
347 trimodal distribution at 18 nm, 53 nm and 150 nm for open-ocean marine Arctic NPF event (Park et al.,
348 2020). Lachlan-Cop et al. (2020) presented k-mean cluster analysis of particle size distribution measured
349 at Halley, Antarctica, showing a nucleation peak at 15 nm for “nucleation” ultrafine category and a
350 nucleation peak at 27 nm for “bursting” ultrafine category.

351 Air mass back trajectories were calculated at hourly intervals to investigate possible source regions
352 for the observed NPF events. Figure 2g shows the residence times of air masses over the three domains.
353 Based on 2-days air mass transport history analysis, air masses allocated to ocean, sea-ice and land
354 account for 83, 12 and 5%, respectively, during the study period. 97 cases were identified as NPF events,
355 80 of which were observed when the air mass originated over the ocean domain (Figure 4). 12 NPF events
356 were observed in air masses originating over the sea-ice domain, while the remaining 5 events were
357 associated with multi-regional origin (3 cases) and land origin (2 cases). Multi-regional origin indicated
358 air masses simultaneously influenced by all three domains. Median BC concentration for ocean, sea-ice,
359 and multiple air masses found to be 23.8 ng m⁻³, 12.7 ng m⁻³, 9.8 ng m⁻³, respectively, (Figure S5),
360 indicating pristine clean air masses with minimum influence from anthropogenic pollutions during each
361 NPF event case. Our results indicated that NPF events were more common in air masses originating over
362 the ocean and sea-ice compared to those originating from the land. Precursors released by both ocean and
363 sea-ice could play an important role in the formation of new particles in the Antarctic atmosphere.

364 **3.1.4. Spatial extension of regional nucleation event**

365 Many previous studies have reported that key steps of the nucleation process (e.g., cluster
366 stabilization) occur in the size range ~2 nm, in line with recent direct observations of atmospheric
367 molecular clusters (Kerminen et al., 2018; Kulmala et al., 2013). However, during NPF events, we did

368 not observe particle formation starting directly from the lower end of the particle size spectrum (2.5 nm),
369 showing that the formation of freshly nucleated particles could not have actually taken place at the site.
370 Indeed, the initial diameter of particles that arrived to the measurement site during the NPF ranged from
371 4 nm to 16 nm (Figure 3a). Median values of NPF event duration (Figure 3b) and growth rate (Figure 3c)
372 were 4.0 hour and 0.83 nm hr^{-1} , respectively. We assumed that they were transported from elsewhere or
373 produced aloft, and detected the appearance of an already grown mode. Consistent with these studies,
374 NPF events can be a regional-scale phenomenon extending over spatial scales of tens to hundreds of
375 kilometers in several regions, such as the remote marine boundary layer (Zheng et al., 2021), Canadian
376 high Arctic (Eureka, Nunavut, on Ellesmere Island in the Canadian Arctic Archipelago) (Tremblay et al.,
377 2019), and Arctic ship-based observations.

378 Assuming the region is characterized by homogenous meteorological conditions, we estimated the
379 spatial scale of NPF by multiplying the time during which a distinct nucleation mode can be observed at
380 the sampling site by the locally measured wind speed (Birmili et al., 2003; Crippa and Pryor, 2013). As
381 shown in Figure 3d, the spatial extend of NPF event associated with substantial particle growth can be
382 16–816 km (median value: 155 km), indicating the large-scale NPF events. Weller et al. (2015) measured
383 size distributions at the coastal Antarctic station Neumayer during two summer campaigns (from 20
384 January to 26 March 2012 and 1 February to 30 April 2014). They found that the spatial extend of NPF
385 event was estimated to be around $170 \pm 85 \text{ km}$, taking into account the prevailing wind velocity (around
386 $8 \pm 4 \text{ m s}^{-1}$) and the confined NPF duration (around 6h).

387

388 **3.2. Case studies**

389 This section presents a detailed overview of the ocean, sea ice, and multi-regional NPF events.

390 **3.2.1. Marine NPF event**

391 A striking series of NPF events took place over seven days (Figure 6), starting at approximately
392 00:00 on December 9, 2018. Events starting at midnight can likely indicate their formation few hours
393 earlier during afternoon sunlight, because the events are observed with an already grown nucleation mode.

394 Time series of meteorological parameters, air mass origins, oceanic biological activity (estimated by
395 chlorophyll and DMSP exposures), particle size distribution (measured by nano-SMPS and standard-
396 SMPS), and CCN concentrations are shown in Figure 6. During this time, the prevailing northerly winds
397 (median 307 °) were stable at 7.7 m s⁻¹. Air temperature varied from -1.5 to 2.1 °C (median 0.5 °C) and
398 RH varied from 75–97% (median 89 %). There were no data for solar radiation during these events. Air
399 masses predominantly traveled over the Antarctic Ocean (46.9, 0.7, and 0.4 h over ocean, land, and sea
400 ice, respectively) and could be categorized as originating from the Antarctic Ocean. Specifically, the air
401 mass originated mainly from Bellingshausen Sea (Figure 5a). During this event, the median total DMSP
402 and chlorophyll exposures in the surface sea were 18 nmol L⁻¹ and 0.26 mg m⁻³, respectively.

403 Between 00:00 and 20:00 on December 9, N_{NUC} increased from 196 to 688 cm⁻³. At the same time,
404 CCN concentrations at 0.4 % supersaturation gradually increased from 138 (00:00 on December 0) to 326
405 cm⁻³ (12:00 on December 11), an increase of 135%. In addition, elevated N_{NUC} occurred at 00:00 on
406 December 13, ranging from 118–522 cm⁻³. CCN number concentration at 0.4% supersaturation began to
407 increase at this time (95 cm⁻³) and reached its maximum at 18:00 (503 cm⁻³), with a concentration increase
408 of 431%.

409

410 3.2.2. Sea-ice NPF event

411 The NPF event with subsequent particle growth were detected from around 19:00 on January 13,
412 2018, to around 08:00 on January 14, 2018 (Figure 7). Air temperature and RH during the event were
413 0.1 °C and 85%, respectively, while solar radiation decreased from 131.7 to 0.2 W m⁻². Winds were mild
414 and stable (1.9–5.7 m s⁻¹), with a prevailing northwesterly (262–350°) direction and air masses
415 predominantly coming from sea-ice. The average retention times of the 2 d back trajectories traveling
416 over ocean, sea-ice, and land were 20.0, 20.9, and 7.1 h, respectively, indicating sea-ice-influenced air
417 masses (Figure 5b). During the NPF event, both total DMSP and chlorophyll exposure values are stable,
418 with median exposures of 13.3 nmol L⁻¹ and 0.2 mg m⁻³, respectively.

419 During the event, CN_{2.5} and CN₁₀ increased to 5669 and 5097 cm⁻³, respectively. Furthermore, the

420 median N_{NUC} , N_{AIT} , and N_{ACC} values were 508, 376, and 66 cm^{-3} , respectively. Elevated CCN
421 concentrations at 0.2 and 0.4 % supersaturations were not observed, whereas CCN concentrations at 0.6,
422 0.8, and 1.0 % supersaturations slightly increased during the event. For instance, CCN concentration at
423 0.8 % supersaturation was 517 cm^{-3} at 20:00 on January 13, then increased to 688 cm^{-3} , until 23:00 on
424 January 13. The CCN concentration at 0.6, 0.8, and 1.0% supersaturations increased by 11%, 33%, and
425 58%, respectively.

426

427 **3.2.3. Multiple NPF event**

428 An intensive NPF event occurred from November 16 to November 17, 2018 (Figure 8). Air
429 temperature during the event ranged from -2.5 to -0.1 °C (median -1.3 °C). RH ranged from 70–95%
430 (median 79%), slightly lower than that for the marine and sea-ice NPF events described above. During
431 the NPF event observed from 20:00 on November 16 to 02:00 on November 17, solar radiation decreased
432 from 30 to 0 W m^{-2} . This suggests that the actual formation and growth occurred during daylight hours
433 upwind from measurement location, but very slow growth continued over the Antarctic Peninsula
434 allowing the detection of observed grown mode at ~ 7 nm after the sunset. Wind speed ranged from 4.3–
435 9.5 m s^{-1} with a constant direction from the southwest (median 239 °). Air mass back trajectories showed
436 multiple origins before reaching the station, passing over ocean (25.7 h, 53% of residence time), sea-ice
437 (12.4 h, 26% of residence time), and land (10.0 h, 21% of residence time) (Figure 5c). During the event,
438 the median total DMSP and chlorophyll exposures in the sea surface were 6.0 nmol L^{-1} and 0.2 mg m^{-3} ,
439 respectively.

440 At the start of the event (17:00 on November 16), N_{NUC} , N_{AIT} , and N_{ACC} were 687, 83, and 13 cm^{-3} ,
441 respectively. The particle number concentration of the nucleation mode sharply increased to 1610 cm^{-3} at
442 the NPF time, and its peak concentration occurred 7 h after the start of the event (00:00 on November 17),
443 indicating spatial extent of the formation region. The peak concentration of Aitken mode particles
444 successively appeared 14 h after the start of the event (07:00 on November 17) and 22 h respectively for
445 accumulation mode particles (15:00 on November 17). The values in the Aitken and accumulation mode

446 ranges were 448 and 92 cm^{-3} , respectively. We also observed a gradual increase in CCN concentration for
447 23 h. CCN concentration at 0.4 % supersaturation increased from 78 (17:00 on November 16) to 272 cm^{-3}
448 (15:00 on November 17). This NPF event may have been a source of CCN, which enhanced CCN
449 concentrations by 248%.

450

451 **3.3. Influence of air mass origin on the NPF event**

452 **3.3.1. Parameters related to NPF**

453 Our results show that NPF and its growth events had largely different features depending on air
454 mass origin (Figure S6). Although only 3 cases of multi-regional NPF events occurred during the pristine
455 and clean periods (not included in Figure 9), the most intense NPF event was observed with multi-regional
456 source region. Here, we compared N_{NUC} , FR GR, and CS, for the ocean and sea-ice air masses (Figure 9
457 a-d). The FR, GR, and CS values agreed well with those reported in previous studies at other Antarctic
458 sites (Järvinen et al., 2013; Kim et al., 2019; Kyrö et al., 2013; Weller et al., 2015), but significantly lower
459 than the values reported by the Quéléver et al. (2022), who showed the average FR and GR were 0.686
460 $\text{cm}^{-3} \text{ s}^{-1}$ and 4.2 nm h^{-1} , respectively. The median N_{NUC} and FR values for the ocean air mass (N_{NUC} : 220
461 cm^{-3} and FR: $1.2 \times 10^{-2} \text{ cm}^{-3} \text{ s}^{-1}$) were 1.6 and 3.0 times lower than those of sea-ice air mass (N_{NUC} : 343
462 cm^{-3} and FR: $3.6 \times 10^{-2} \text{ cm}^{-3} \text{ s}^{-1}$), respectively. This implies that marine NPF events are frequent, but
463 weak in terms of N_{NUC} and FR values. Unlike N_{NUC} and FR, there were no marked differences between
464 the median values of GR and CS by air mass category. The median particle GR values for ocean, sea-ice,
465 and multiple air masses were 0.8, 0.7, and 0.9 nm h^{-1} , respectively. In comparison, Jokinen et al. (2018)
466 reported that GR values ranged from 0.3 to 1.3 nm h^{-1} at Aboa, and Brean et al. (2021) showed GR of 0.4
467 to 0.6 nm h^{-1} measured during the PI-ICE cruise. To examine the effects of oceanic biological activity on
468 NPF properties, we examined solar radiation intensity, chlorophyll exposure and DMSP exposure for the
469 two air mass (or source region) categories (Figure 9 e-g). **There was no difference in the median value in**
470 **solar radiation, while the median values for chlorophyll exposure and DMSP exposure were higher in air**

471 masses originating from the ocean than in air masses originating from the sea ice. The median chlorophyll
472 exposure in ocean-influenced air masses (0.2 mg m^{-3}) was roughly twice that of the sea-ice-influenced air
473 mass (0.1 mg m^{-3}). Total DMSP exposure for the ocean-influenced air mass was ~ 2.7 times that of the
474 sea-ice air mass.

475

476 3.3.2. Potential sources facilitating new particle formation

477 The chlorophyll exposure and DMSP exposure during marine NPF events were higher than those
478 during sea ice NPF events, suggesting a large chance to carry biologically-derived organic compounds
479 from the open ocean areas to the observation site. DMSP, a metabolite of oceanic phytoplankton, is partly
480 converted into gaseous DMS through enzymatic cleavage (Simó, 2001), which is the largest natural sulfur
481 source in the atmosphere (Barnes et al., 2006). Hence, the photooxidation products of biogenic DMS in
482 the Antarctic atmosphere (e.g., Sulfuric acid and Methane sulfonic acid) could be a major contributor to
483 NPF and its growth when the air mass originates from the ocean. Jang et al. (2019) reported that NPF
484 events were more frequent in air masses originating from the Bellingshausen Sea than the Weddell Sea
485 during the biologically productive austral summer, and it is likely that the taxonomic composition of
486 phytoplankton can be related to the formation of new particles in the Antarctic Ocean. Biogenic DMS
487 was found to be a precursor of NPF in coastal Antarctica (Yu and Luo, 2010).

488 The air mass exposure to chlorophyll and DMSP for sea-ice NPF events were 1.8 and 2.7 times
489 lower than those of marine NPF events. This could be explained by volatile iodine compounds released
490 from ice-covered areas in Antarctica (Jokinen et al; 2018; Saiz-Lopez et al., 2007; Sipilä et al., 2016);
491 however, iodine compounds were not measured during our study period. Previously, iodine compounds
492 were found in large concentrations in and above the sea-ice of the Weddell Sea in Antarctica during spring
493 and summer (Atkinson et al., 2012). Roscoe et al. (2015) also confirmed that iodine compounds may
494 contribute to the secondary production of a significant number of particles measured at Halley and
495 Neumayer on the Antarctic coast.

496 In our study, sea-ice NPF events occurred frequently in January (middle of austral summer) and

497 September (early austral spring) (Figure 4). We compared the JR, GR, and CS values for the sea-ice NPF
498 cases observed between January and September (Figure S7) because of their notable differences in ice
499 coverage. In Antarctica, the minimum ice coverage is observed in February and the maximum in
500 September (Parkinson and Cavalieri, 2012). Our results showed that JR, GR, and CS values were much
501 higher in January than in September, indicating different NPF processes. The January events occurred
502 under low ice-coverage conditions, similar to previous studies from polar areas such as Svalbard
503 (Dall'Osto et al., 2017) and Greenland (Dall'Osto et al., 2018). Both studies showed that NPF events are
504 related to biogenic precursors released by open water and melting sea-ice regions, particularly during the
505 summer. In contrast, the September events occurred under high ice-coverage conditions. The monthly
506 median values of solar radiation showed that solar radiation intensity was very low from May to August
507 and then started to increase from September (Table 1). During the September events, median solar
508 radiation intensity was found to be 63 W m^{-2} . It is therefore possible that elevated sea-ice concentrations
509 under sufficient solar radiation around Antarctica lead to an increase in the concentration of halogen
510 species, resulting in the production of newly formed particles.

511 The most intensive NPF event was observed in multiple air masses, although the oceanic biological
512 activity was lower than that in the oceanic air mass. This indicated that terrestrial sources from continental
513 Antarctica, in addition to both DMS (mainly from the ocean) and iodine (mainly from sea-ice), may have
514 contributed to NPF. First, previous studies have reported that precursors emitted from seabird colonies
515 are linked to NPF (Schmale et al., 2013; Weber et al., 1998). The Chottaebawi area in the southwestern
516 part of King George Island (around 2 km away from our observation site) is an important penguin colony
517 in the Antarctic region (Lee et al., 2009), while the cape area near King Sejong Station is abundantly
518 populated by flying seabirds such as skua. Given the proximity and abundance of seabird colonies at King
519 Sejong Station, [seabird colony emissions are the likely sources of precursor gases to NPF \(e.g., ammonia
520 and amine\) \(Quéléver et al., 2022\)](#). In fact, 2 NPF events (4 February 2018 for marine air mass origin and
521 18 February 2018 for multiple air mass origin) were observed when winds were seen to originate from
522 the south sector where strong emission from the penguin colonies (southeast sector of $106\text{--}140^\circ$). Figure

523 S8 showed the contour plots of the size distributions and wind roses during those days. Although we did
524 not directly measure the precursor gases such as ammonia and amine that can trigger the NPF, we can
525 speculate that the fauna on the land or at the shore such as penguin and seabird colonies could not be
526 excluded as the potential source of NPF events locally although highly productive and ice melting
527 Weddell sea is coinciding with southeast direction too. Previous studies reported that precursor gases for
528 NPF (e.g., ammonia) can originate from the decomposition of excreta from seabirds and penguins
529 (Lachlan-Cope et al., 2020; Legrand et al., 1998; Liu et al., 2018; Schmale et al., 2013). More recently,
530 Quéléver et al. (2022) proposed that nitrogen-containing species could be land-sourced (e.g., from a high
531 penguin population during the summertime) or marine-sourced (e.g., from the biological activity of
532 plankton in the ocean and melting sea ice). The ammonia from seabird-colony guano is a key factor
533 contributing to bursts of newly formed particles, which are observed in the summertime Arctic (Croft et
534 al., 2016). Second, biogenic emissions from vegetation in the Antarctic Peninsula, mainly composed of
535 relatively small and sparse patches of lichens and mosses (Miranda et al., 2020), could be associated with
536 NPF and growth. Kim et al. (2006) studied plant communities on the Barton Peninsula around King
537 Sejong Station in the maritime Antarctic and concluded that ~47% of the investigated area was covered
538 by vegetation although generally sparse. Finally, biogenic precursors from meltwater ponds in continental
539 Antarctica have also been suggested (Kyrö et al., 2013) as a possible source of aerosol production (Weller
540 et al., 2018). Overall, our data suggest that complex interconnected ecosystems across ocean, sea ice, and
541 land can lead to an enhancement in Antarctic NPF.

542 **3.3.3. NPF as a source of CCN**

543 For a given SS of 0.4%, the median CCN number concentrations were rather similar 184, 144, and
544 178 cm⁻³ for ocean, sea ice, and multiple air masses, respectively (Figure 9h). The values are in line with
545 previous studies published from the Antarctic regions. Humphries et al. (2023) reported CCN
546 concentrations nearby East Antarctic observations from Macquarie Island and Kennaook / Cape Grim as
547 well as recent ship voyages of the RSV *Aurora Australis* and the RV *Investigator* in the region. The median
548 CCN value at a SS of 0.5% was in the ranges of 88–145 cm⁻³ at Macquarie Island, 57–158 cm⁻³ at

549 Kennaook / Cape Grim, and 40–230 cm⁻³ during the voyages (No voyage data exist for the winter months),
550 respectively. The PCAN project exhibited that a median particle number concentration larger than 3 nm
551 of 354 cm⁻³ was observed from the voyage and median CCN at 0.55 % supersaturation were 167 cm⁻³,
552 implying approximately half the particles measured as CN₃ could be activated as CCN (Simmons et al.,
553 2021). Recently, several ship-based measurements over the Southern Ocean found significantly increased
554 MSA concentrations in air masses originating close to the Antarctic coastline, alongside enhancements in
555 CCN concentration (Humphries et al., 2021). Of the 83 NPF events, CCN concentrations increased by 2–
556 268% (median 44%) following 1 to 36 hours (median 8 hours) after NPF events. The median increase in
557 CCN concentrations was 44 %, 34 %, and 107 % for ocean, sea ice, and multiple air masses, respectively.
558 NPF can be an important source of CCN in Antarctica, and the highest CCN enhancement was observed
559 when air masses passed through multiple regions, followed by ocean and sea-ice regions. Our results
560 provide the first direct evidence of CCN production resulting from an NPF event in the Antarctic
561 atmosphere, based on simultaneous measurements of particle number size distribution (e.g., diameter
562 ranges of 2.5–300 nm) and CCN number concentrations in real time throughout the year.

563 We also compared CCN activity and critical diameter for the three selected periods (Figure 9i and
564 j). The median values of CCN activity, i.e. the ratio of the number concentration of particles that activated
565 to become CCN at a given supersaturation to the total number concentration or particles larger than 10
566 nm (CN₁₀), were similar (about 5%) in three different air masses. The critical diameter (D_c), the diameter
567 at which the integration of aerosol size distribution from the largest particle diameter to the lowest one
568 matches the measured CCN concentration, was determined using the measured aerosol size distribution,
569 CN₁₀, and CCN concentrations (Furutani et al., 2018). The median D_c value at 0.4% supersaturation was
570 estimated to be 41 nm, 32 nm, and 37 nm for ocean, sea ice, and multiple air masses, respectively. These
571 results agreed well with those reported in previous studies that determined D_c at the Finnish Antarctic
572 Research Station, Aboa (Kyrö et al., 2013), a clean subarctic background site (Komppula et al., 2005),
573 and over remote Southern Ocean around Antarctica (Fossum et al., 2018; Fossum et al., 2020). For
574 instance, Kyrö et al. (2013) found the smallest D_c at 48 nm. The median D_c , as suggested by Komppula

575 et al. (2005), varied from 50–128 nm (average 80 nm). The D_c value for maritime polar and marine
576 modified continental Antarctic air masses were 71 and 59 nm, respectively (Fossum et al., 2020).

577 A time series of daily mean CCN concentrations at five different supersaturation ratio of 0.2, 0.4,
578 0.6, 0.8, and 1 was illustrated in Figure S10. To understand the contribution of growing particles on the
579 CCN concentrations during NPF event, we determined the increase in CCN concentration during growth
580 periods (i.e., growth to smaller than 40 nm particles and growth to larger than 40 nm particles) compared
581 to baseline values under different supersaturation conditions (Figure 10), according to the method
582 suggested by Chang et al. (2022). When particle growth was smaller than to 40 nm (growth \leq 40 nm), the
583 mean CCN concentrations increased by 59–178 cm^{-3} for a SS of 0.2 %–1.0 %, representing a 172–217 %
584 increase compared to the values during baseline conditions. When particle growth was larger than to 40
585 nm (growth $>$ 40 nm), the mean CCN concentrations increased by 57–227 cm^{-3} for a SS of 0.2 %–1.0 %,
586 representing a 170–249 % increase compared to baseline values. Our results indicate that particles formed
587 from NPF events can lead to the significantly enhanced CCN concentration in Antarctic Peninsula, and
588 this effect is more pronounced if we consider particle growth larger than 40 nm, consistent with ship-
589 based observations (Chang et al., 2022) and aircraft-based observation (Willis et al., 2016) in the Canadian
590 Arctic during summer.

591

592 **4. Conclusions**

593 We measured the number size distribution of 2.5–300 nm particles and CCN number concentrations
594 at King Sejong Station in the Antarctic Peninsula continuously from January 1 to December 31, 2018.
595 The annual median values of N_{NUC} , N_{AIT} , and N_{ACC} were 46.8 cm^{-3} , 53.5 cm^{-3} , and 21.7 cm^{-3} , respectively.
596 Overall, clear annual and seasonal patterns of particle number concentrations in all size classes were
597 observed (high concentrations in summer and low concentrations in winter). Furthermore, the monthly
598 CN_{10} value was positively correlated with the monthly N_{NUC} , implying that summer maximum particle
599 concentrations could be largely influenced by newly formed particles in the Antarctic atmosphere. Among
600 meteorological parameters, the elevated N_{NUC} values (i.e., indicators of NPF events) were more likely to

601 be accompanied by high solar radiation, high temperature, and low RH, regardless of wind speed.

602 NPF events were identified based on size distribution data measured using two SMPSs. During the
603 pristine and clean periods, 97 events (26% of observation days) with elevated N_{NUC} were observed. NPF
604 events occurred more frequently in summer than in any other season. Based on air mass back-trajectory
605 analysis, we distinguished three different types of NPF events: marine (80 cases), sea ice (12 cases), and
606 multiple (3 cases). Marine NPF events were frequent and weak (N_{NUC} , 220 cm^{-3} ; $\text{FR} = 1.2 \times 10^{-2} \text{ cm}^{-3} \text{ s}^{-1}$;
607 $\text{GR} = 0.8 \text{ nm hr}^{-1}$) and occurred when the air mass exposure to oceanic phytoplankton was high
608 (chlorophyll, 0.2 mg m^{-3} ; DMSP, 18 nmol L^{-1}). The photooxidation of biogenic DMS in the Antarctic
609 atmosphere could be a major contributor to marine NPF events. In contrast, sea-ice NPF events (N_{NUC} ,
610 343 cm^{-3} ; FR , $3.6 \times 10^{-2} \text{ cm}^{-3} \text{ s}^{-1}$; GR , 0.7 nm h^{-1}) were observed when the air mass exposure to oceanic
611 phytoplankton was relatively low (chlorophyll, 0.1 mg m^{-3} ; DMSP, 7 nmol L^{-1}), which may be due to
612 volatile iodine compounds released from ice-covered areas. Strong NPF events (N_{NUC} , 516 cm^{-3} ; FR , 3.2
613 $\times 10^{-2} \text{ cm}^{-3} \text{ s}^{-1}$; GR , 0.9 nm hr^{-1}) were associated with multiple air masses, indicating complex
614 interconnected ecosystems leading to an enhancement in Antarctic NPF.

615 To investigate the connection between newly formed particles and CCN production, we compared
616 CCN properties for the three air mass categories. The median CCN number concentrations at a given SS
617 of 0.4% were 184, 144, and 178 cm^{-3} for ocean, sea ice, and multiple air masses, respectively. Of the 83
618 events, an increase in CCN concentrations after the NPF events was detected, ranging from 2–268 %
619 (median 44 %). The median increase in CCN concentrations was 44 %, 34 %, and 107 % for ocean, sea
620 ice, and multiple air masses, respectively. NPF events led to increased CCN concentrations at King Sejong
621 Station. The median value of D_c at a supersaturation of 0.4% was estimated to be 41 nm, 32 nm, and 37
622 nm for ocean, sea ice, and multiple air masses, respectively. This study is the first to report CCN
623 production resulting from Antarctic NPF events in the Antarctic Peninsula. However, further detailed
624 measurements of the chemical properties of aerosol particles and precursor gases (e.g., ammonia) during
625 NPF events are required to better understand the contribution of these compounds to the formation and
626 growth of aerosol particles and to explore their impacts on CCN formation in the remote Antarctic

627 environment.

628

629 **Data availability**

630 The data analyzed in this publication will be readily provided upon request to the corresponding author
631 (yjyoon@kopri.re.kr).

632

633 **Author contributions**

634 JP and YJY designed the study. JP, HK, YG, EJ, K-TP, SP, and YJY analyzed data. JP wrote the
635 manuscript. CHJ, DC, and CO'D all commented on and discussed the manuscript.

636

637 **Competing interests**

638 The authors declare that they have no conflict of interest.

639

640 **Acknowledgments**

641 We would like to thank the many technicians and scientists of the overwintering crews. This work was
642 supported by the KOPRI project (PE23030).

643

644 **References**

- 645 Asmi, E., Frey, A., Virkkula, A., Ehn, M., Manninen, H. E., Timonen, H., Tolonen-Kivimäki, O., Aurela,
646 M., Hillamo, R., and Kulmala, M.: Hygroscopicity and chemical composition of Antarctic sub-
647 micrometre aerosol particles and observations of new particle formation, *Atmos. Chem. Phys.*, 10,
648 4253–4271, <https://doi.org/10.5194/acp-10-4253-2010>, 2010.
- 649 Asmi, E., Neitola, K., Teinila, K., Rodriguez, E., Virkkula, A., Backman, J., Bloss, M., Jokela, J.,
650 Lihavainen, H., De Leeuw, G., Paatero, J., Aaltonen, V., Mei, M., Gambarte, G., Copes, G., Albertini,
651 M., Fogwill, G. P., Ferrara, J., Barlasina, M. E., and Sanchez, R.: Primary sources control the
652 variability of aerosol optical properties in the Antarctic Peninsula, *Tellus B*, 70, 1,
653 <https://doi.org/10.1080/16000889.2017.1414571>, 2018.
- 654 Atkinson, H. M., R.-J. Huang, R. Chance, H. K. Roscoe, C. Hughes, B. avison, A. Schönhardt, A. S.
655 Mahajan, A. Saiz-Lopez, and P. S. Liss (2012), Iodine emissions from the sea ice of the Weddell
656 Sea, *Atmos. Chem. Phys.*, 12, 11,229–11,244, doi:10.5194/acp-12-11229-2012.
- 657 Barnes, I., Hjorth, J., and Mihalopoulos, N.: Dimethyl sulfide and dimethyl sulfoxide and their oxidation
658 in the atmosphere, *Chem. Rev.*, 106, 940–975, 2006.
- 659 Belosi, F., Contini, D., Donato, A., Santachiara, G., and Prodi, F.: Aerosol size distribution at Nansen Ice
660 Sheet Antarctica, *Atmos. Res.*, 107, 42–50, 2012.
- 661 Birmili, W., Berresheim, H., Plass-Dülmer, C., Elste, T., Gilge, S., Wiedensohler, A., and Uhrner, U.: The
662 Hohenpeissenberg aerosol formation experiment (HAFEX): a long-term study including size-
663 resolved aerosol, H₂SO₄, OH, and monoterpenes measurements, *Atmos. Chem. Phys.*, 3, 361–376,
664 <https://doi.org/10.5194/acp-3-361-2003>, 2003.

- 665 Brean, J., Dall'Osto, M., Simó, R., Shi, Z., Beddows, D. C. S., and Harrison, R. M.: Open ocean and
666 coastal new particle formation from sulfuric acid and amines around the Antarctic Peninsula, *Nat.*
667 *Geosci.*, 14, 383–388, <https://doi.org/10.1038/s41561-021-00751-y>, 2021.
- 668 Buenrostro Mazon S., Kontkanen J., Manninen H.E., Nieminen T., Kerminen V.-K. & Kulmala M. 2016:
669 A long-term comparison of nighttime cluster events and daytime ion formation in a boreal forest.
670 *Boreal Env. Res.* 21: 242–261.
- 671 Carslaw, K. S., Lee, L. A., Reddington, C. L., Pringle, K. J., Rap, A., Forster, P. M., Mann, G. W.,
672 Spracklen, D. V., Woodhouse, M. T., Regayre, L. A., and Pierce, J. R.: Large contribution of natural
673 aerosols to uncertainty in indirect forcing, *Nature*, 503, 67–71, doi:10.1038/nature12674, 2013.
- 674 Chang, R. Y.-W., Abbatt, J. P. D., Boyer, M. C., Chaubey, J. P., and Collins, D. B.: Characterizing the
675 hygroscopicity of growing particles in the Canadian Arctic summer, *Atmos. Chem. Phys.*, 22, 8059–
676 8071, <https://doi.org/10.5194/acp-22-8059-2022>, 2022.
- 677 Chen, J. L., Wilson, C. R., Blankenship, D., and Tapley, B. D.: Accelerated Antarctic ice loss from satellite
678 gravity measurements, *Nat. Geosci.*, 2, 859–862, 2009.
- 679 Chen, D. R., Pui, D. Y. H., Hummes, D., Fissan, H., Quant, F. R., and Sem, G. J.: Design and evaluation
680 of a nanometer aerosol differential mobility analyzer (Nano-DMA), *J. Aerosol. Sci.*, 29, 497–509,
681 doi:10.1016/S0021-8502(97)10018-0, 1998.
- 682 Collins, D. B., Burkart, J., Chang, R. Y.-W., Lizotte, M., Boivin-Rioux, A., Blais, M., Mungall, E. L.,
683 Boyer, M., Irish, V.E., Massé, G., Kunkel, D., Tremblay, J.-É., Papakyriakou, T., Bertram, A. K.,
684 Bozem, H., Gosselin, M., Lévasseur, M., and Abbatt, J. P. D.: Frequent ultrafine particle formation
685 and growth in Canadian Arctic marine and coastal environments, *Atmos. Chem. Phys.*, 17, 13119–
686 13138, <https://doi.org/10.5194/acp-17-13119-2017>, 2017.
- 687 Croft, B., Wentworth, G. R., Martin, R. V., Leitch, W. R., Murphy, J. G., Murphy, B. N., Kodros, J. K.,
688 Abbatt, J. P. D., and Pierce, J. R.: Contribution of Arctic seabird-colony ammonia to atmospheric
689 particles and cloud-albedo radiative effect, *Nat. Commun.*, 7, 13444,
690 <https://doi.org/10.1038/ncomms13444>, 2016.
- 691 Crippa, P. and Pryor, S. C.: Spatial and temporal scales of new particle formation events in eastern North
692 America, *Atmos. Environ.*, 75, 257–264, <https://doi.org/10.1016/j.atmosenv.2013.04.051>, 2013
- 693 Dada, L., Paasonen, P., Nieminen, T., Buenrostro Mazon, S., Kontkanen, J., Peräkylä, O., Lehtipalo, K.,
694 Hussein, T., Petäjä, T., Kerminen, V. M., Bäck, J., and Kulmala, M.: Long-term analysis of clear-
695 sky new particle formation events and nonevents in Hyytiälä, *Atmos. Chem. Phys.*, 17(10), 6227–
696 6241, doi:10.5194/acp-17-6227-2017, 2017.
- 697 Dall'Osto, M., Sotomayor-Garcia, A., Cabrera-Brufau, M., Berdalet, E., Vaque', D., Zeppenfeld, S., van
698 Pinxteren, M., Herrmann, H., Wex, H., Rinaldi, M., Paglione, M., Beddows, D., Harrison, R., Avila,
699 C., Martin-Martin, R.P., Park, J., Barbosa, A.: Leaching material from Antarctic seaweeds and
700 penguin guano affects cloud-relevant aerosol production, *Sci. Total Environ.* 831, 154772,
701 <http://dx.doi.org/10.1016/j.scitotenv.2022.154772>, 2022.
- 702 Dall'Osto, M., Ovadnevaite, J., Paglione, M., Beddows, D. C. S., Ceburnis, D., Cree, C., Cortes, P.,
703 Zamanillo, M., Nunes, S. O., Perez, G. L., Ortega-Retuerta, E., Emelianov, M., Vaque, D., Marrase,
704 C., Estrada, M., Sala, M. M., Vidal, M., Fitzsimons, M. F., Beale, R., Airs, R., Rinaldi, M., Decesari,
705 S., Facchini, M. C., Harrison, R. M., O'Dowd, C., and Simo, R.: Antarctic sea ice region as a source
706 of biogenic organic nitrogen in aerosols, *Sci. Rep.*, 7, 6047, <https://doi.org/10.1038/s41598-017-06188-x>, 2017.
- 708 Dall'Osto, M., Beddows, D. C. S., Tunved, P., Krejci, R., Ström, J., Hansson, H.-C., Yoon, Y. J., Park, K.-
709 T., Becagli, S., Udisti, R., Onasch, T., O'Dowd, C. D., Simó, R., and Harrison, R. M.: Arctic sea ice
710 melt leads to atmospheric new particle formation, *Sci. Rep.*, 7, 3318,
711 <https://doi.org/10.1038/s41598-017-03328-1>, 2017.
- 712 Dall'Osto, M., Geels, C., Beddows, D. C. S., Boertmann, D., Lange, R., Nøjgaard, J. K., Harrison Roy,
713 M., Simo, R., Skov, H., and Massling, A.: Regions of open water and melting sea ice drive new
714 particle formation in North East Greenland, *Sci. Rep.*, 8, 6109, <https://doi.org/10.1038/s41598-018-24426-8>, 2018.

716 Dal Maso, M.: Condensation and coagulation sinks and formation of nucleation mode particles in coastal
717 and boreal forest boundary layers, *J. Geophys. Res.*, 107, 8097,
718 <https://doi.org/10.1029/2001jd001053>, 2002

719 Dal Maso, M., Kulmala, M., Riipinen, I., Wagner, R., Hussein T., Aalto, P. P., and Lehtinen, K. E. J.:
720 Formation and growth of fresh atmospheric aerosols: eight years of aerosol size distribution data
721 from SMEAR II, Hyytiälä, Finland, *Boreal Environ. Res.*, 10, 323–336, 2005.

722 Decesari, S., Paglione, M., Rinaldi, M., Dall'Osto, M., Simó, R., Zanca, N., Volpi, F., Facchini, M. C.,
723 Hoffmann, T., Götz, S., Kampf, C. J., O'Dowd, C., Ceburnis, D., Ovadnevaite, J., and Tagliavini,
724 E.: Shipborne measurements of Antarctic submicron organic aerosols: an NMR perspective linking
725 multiple sources and bioregions, *Atmos. Chem. Phys.*, 20, 4193–4207, [https://doi.org/10.5194/acp-](https://doi.org/10.5194/acp-20-4193-2020)
726 [20-4193-2020](https://doi.org/10.5194/acp-20-4193-2020), 2020.

727 Draxler, R. R. and Hess, G. D.: An overview of the HYSPLIT_4modelling system for trajectories, *Aust.*
728 *Meteorol. Mag.*, 47, 295–308, 1998.

729 Ehn, M., Vuollekoski, H., Petäjä, T., Kerminen, V.-M., Vana, M., Aalto, P., de Leeuw, G., Ceburnis, D.,
730 Dupuy, R., O'Dowd, C. D., and Kulmala, M.: Growth rates during coastal and marine new particle
731 formation in western Ireland, *J. Geophys. Res.-Atmos.*, 115, D18218,
732 <https://doi.org/10.1029/2010JD014292>, 2010.

733 Fiebig, M., Hirdman, D., Lunder, C. R., Ogren, J. A., Solberg, S., Stohl, A., and Thompson, R. L.: Annual
734 cycle of Antarctic baseline aerosol: controlled by photooxidation-limited aerosol formation, *Atmos.*
735 *Chem. Phys.*, 14, 3083–3093, <https://doi.org/10.5194/acp-14-3083-2014>, 2014.

736 Fiebig, M., Lunder, C. R., and Stohl, A.: Tracing biomass burning aerosol from South America to Troll
737 Research Station, Antarctica, *Geophys. Res. Lett.*, 36, L14815, doi:10.1029/2009GL038531, 2009.

738 Fossum, K. N., Ovadnevaite, J., Ceburnis, D., Dall'Osto, M., Marullo, S., Bellacicco, M., Simó, R., Liu,
739 D., Flynn, M., Zuend, A., and O'Dowd, C.: Summertime primary and secondary contributions to
740 Southern Ocean cloud condensation nuclei, *Sci. Rep.*, 8, 13844, [https://doi.org/10.1038/s41598-](https://doi.org/10.1038/s41598-018-32047-4)
741 [018-32047-4](https://doi.org/10.1038/s41598-018-32047-4), 2018.

742 Fossum, K. N., Ovadnevaite, J., Ceburnis, D., Preißler, J., Snider, J. R., Huang, R. -J., Zuend, A., and
743 O'Dowd, C.: Sea-spray regulates sulfate cloud droplet activation over oceans, *npj Clim. Atmos.*
744 *Sci.*, 3, 14, <https://doi.org/10.1038/s41612-020-0116-2>, 2020.

745 Furutani, H., Dall'osto, M., Roberts, G. C., and Prather, K. A.: Assessment of the relative importance of
746 atmospheric aging on CCN activity derived from field observations, *Atmos. Environ.*, 42, 3130–
747 3142, 2008.

748 Galí, M., Devred, E., Lévassieur, M., Royer, S.-J., and Babin, M.: A remote sensing algorithm for
749 planktonic dimethylsulfoniopropionate (an analysis of global patterns, *Remote Sens. Environ.*, 171,
750 171–184, <https://doi.org/10.1016/j.rse.2015.10.012>, 2015.

751 Giordano, M. R., Kalnajs, L. E., Avery, A., Goetz, J. D., Davis, S. M., and DeCarlo, P. F.: A missing source
752 of aerosols in Antarctica – beyond long-range transport, phytoplankton, and photochemistry, *Atmos.*
753 *Chem. Phys.*, 17, 1–20, <https://doi.org/10.5194/acp-17-1-2017>, 2017

754 Giordano, M. R., Kalnajs, L. E., Goetz, J. D., Avery, A. M., Katz, E., May, N. W., Leemon, A., Mattson,
755 C., Pratt, K. A., and DeCarlo, P. F.: The importance of blowing snow to halogencontaining aerosol
756 in coastal Antarctica: influence of source region versus wind speed, *Atmos. Chem. Phys.*, 18,
757 16689–16711, <https://doi.org/10.5194/acp-18-16689-2018>, 2018.

758 Gras, J. L. and Keywood, M.: Cloud condensation nuclei over the Southern Ocean: wind dependence and
759 seasonal cycles, *Atmos. Chem. Phys.*, 17, 4419–4432, <https://doi.org/10.5194/acp-17-4419-2017>,
760 2017.

761 Grigas, T., Ovadnevaite, J., Ceburnis, D., Moran, E., McGovern, F. M., Jennings, S. G., and O'Dowd, C.:
762 Sophisticated clean air strategies required to mitigate against particulate organic pollution, *Sci. Rep.*,
763 7, 44737, <https://doi.org/10.1038/srep44737>, 2017.

764 Hamed, A., Korhonen, H., Sihto, S.-L., Joutsensaari, J., Jarvinen, H., Petaja, T., Arnold, F., Nieminen, T.,
765 Kulmala, M., Smith, J. N., Lehtinen, K. E. J., and Laaksonen, A.: The role of relative humidity in
766 continental new particle formation, *J. Geophys. Res.*, 116, D03202,

- 767 <https://doi.org/10.1029/2010JD014186>, 2011.
- 768 Hara, K., Sudo, K., Ohnishi, T., Osada, K., Yabuki, M., Shiobara, M., and Yamanouchi, T.: Seasonal
769 features and origins of carbonaceous aerosols at Syowa Station, coastal Antarctica, *Atmos. Chem.*
770 *Phys.*, 19, 7817–7837, <https://doi.org/10.5194/acp-19-7817-2019>, 2019.
- 771 Hara, K., Osada, K., Nishita-Hara, C., and Yamanouchi, T.: Seasonal variations and vertical features of
772 aerosol particles in the Antarctic troposphere, *Atmos. Chem. Phys.*, 11, 5471–5484,
773 <https://doi.org/10.5194/acp-11-5471-2011>, 2011.
- 774 Herenz, P., Wex, H., Mangold, A., Laffineur, Q., Gorodetskaya, I. V., Fleming, Z. L., Panagi, M., and
775 Stratmann, F.: CCN measurements at the Princess Elisabeth Antarctica research station during three
776 austral summers, *Atmos. Chem. Phys.*, 19, 275–294, <https://doi.org/10.5194/acp-19-275-2019>,
777 2019.
- 778 Humphries, R. S., Keywood, M. D., Ward, J. P., Harnwell, J., Alexander, S. P., Klekociuk, A. R., Hara,
779 K., McRobert, I. M., Protat, A., Alroe, J., Cravigan, L. T., Miljevic, B., Ristovski, Z. D., Schofield,
780 R., Wilson, S. R., Flynn, C. J., Kulkarni, G. R., Mace, G. G., McFarquhar, G. M., Chambers, S. D.,
781 Williams, A. G., and Griffiths, A. D.: Measurement report: Understanding the seasonal cycle of
782 Southern Ocean aerosols, *Atmos. Chem. Phys.*, 23, 3749–3777, <https://doi.org/10.5194/acp-23-3749-2023>, 2023.
- 784 Humphries, R. S., Keywood, M. D., Gribben, S., McRobert, I. M., Ward, J. P., Selleck, P., Taylor, S.,
785 Harnwell, J., Flynn, C., Kulkarni, G. R., Mace, G. G., Protat, A., Alexander, S. P., and McFarquhar,
786 G.: Southern Ocean latitudinal gradients of cloud condensation nuclei, *Atmos. Chem. Phys.*, 21,
787 12757–12782, <https://doi.org/10.5194/acp-21-12757-2021>, 2021.
- 788 Humphries, R. S., Schofield, R., Keywood, M. D., Ward, J., Pierce, J. R., Gionfriddo, C. M., Tate, M. T.,
789 Krabbenhoft, D. P., Galbally, I. E., Molloy, S. B., Klekociuk, A. R., Johnston, P. V., Kreher, K.,
790 Thomas, A. J., Robinson, A. D., Harris, N. R. P., Johnson, R., and Wilson, S. R.: Boundary layer
791 new particle formation over East Antarctic sea ice – possible Hg-driven nucleation?, *Atmos. Chem.*
792 *Phys.*, 15, 13339–13364, <https://doi.org/10.5194/acp-15-13339-2015>, 2015.
- 793 Humphries, R. S., Klekociuk, A. R., Schofield, R., Keywood, M., Ward, J., and Wilson, S. R.:
794 Unexpectedly high ultrafine aerosol concentrations above East Antarctic sea ice, *Atmos. Chem.*
795 *Phys.*, 16, 2185–2206, <https://doi.org/10.5194/acp-16-2185-2016>, 2016.
- 796 IPCC: Climate change 2013: The physical science basis, Intergovernmental panel on Climate Change,
797 Cambridge University Press, New York, USA, 571–740, 2013.
- 798 Ito, T.: Size distribution of Antarctic submicron aerosols, *Tellus B*, 45, 145–59, 1993.
- 799 Jang, E., Park, K.-T., Yoon, Y. J., Kim, T.-W., Hong, S.-B., Becagli, S., raversi, R., Kim, J., and Gim, Y.:
800 New particle formation events observed at the King Sejong Station, Antarctic Peninsula – Part 2:
801 Link with the oceanic biological activities, *Atmos. Chem. Phys.*, 19, 7595–7608,
802 <https://doi.org/10.5194/acp-19-7595-2019>, 2019.
- 803 Jang, E., Park, K.-T., Yoon, Y.J., Kim, K., Gim, Y., Chung, H.Y., Lee, K., Choi, J., Park, J., Park, S.-J.,
804 Koo, J.-H., Fernandez, R.P., and Saiz-Lopez, A.: First-year sea ice leads to an increase in dimethyl
805 sulfide-induced particle formation in the Antarctic Peninsula, *Sci. Total Environ.*, 803, 150002.
806 <https://doi.org/10.1016/j.scitotenv.2021.150002>, 2022.
- 807 Jeong, C. H., Hopke, P. K., Chalupa, D. . and Utell, M. : Characteristics of nucleation and growth events
808 of ultrafine particles measured in Rochester, N.Y., *Environ. Sci. Technol.*, 38, 1933–1940, 2004.
- 809 Jeong, C.-H. H., Evans, G. J., McGuire, M. L., Y.-W. Chang, R., Abbatt, J. P. D. D., Zeromskiene, K.,
810 Mozurkewich, M., Li, S.-M. M., Leitch, W. R., Chang, R. Y.-W., Abbatt, J. P. D. D., Zeromskiene,
811 K., Mozurkewich, M., Li, S.-M. M. and Leitch, W. R.: Particle formation and growth at five rural
812 and urban sites, *Atmos. Chem. Phys.*, 10(16), 7979–7995, doi:10.5194/acp-10-7979-2010, 2010.
- 813 Järvinen, E., Virkkula, A., Nieminen, T., Aalto, P. P., Asmi, E., Lanconelli, C., Busetto, M., Lupi, A.,
814 Schioppo, R., Vitale, V., Mazzola, M., Petäjä, T., Kerminen, V.-M., and Kulmala, M.: Seasonal cycle
815 and modal structure of particle number size distribution at Dome C, Antarctica, *Atmos. Chem. Phys.*,
816 13, 7473–7487, <https://doi.org/10.5194/acp-13-7473-2013>, 2013.
- 817 Jokinen, T., Sipilä, M., Kontkanen, J., Vakkari, V., Tisler, P., Duplissy, E.-M., Junninen, H., Kangasluoma,

- 818 J., Manninen, H. E., Petäjä, T., Kulmala, M., Worsnop, D. R., Kirkby, J., Virkkula, A., and Kerminen,
819 V.-M.: Ion-induced sulfuric acid–ammonia nucleation drives particle formation in coastal
820 Antarctica, *Sci. Adv.*, 4, eaat9744, <https://doi.org/10.1126/sciadv.aat9744>, 2018.
- 822 Kerminen, V.-M., Chen, X., Vakkari, V., Petäjä, T., Kulmala, M., and Bianchi, F.: Atmospheric new
823 particle formation and growth: review of field observations, *Environ. Res. Lett.*, 13, 103003,
824 <https://doi.org/10.1088/1748-9326/aadf3c>, 2018.
- 825 Kim, J., Yoon, Y. J., Gim, Y., Kang, H. J., Choi, J. H., Park, K.-T., and Lee, B. Y.: Seasonal variations in
826 physical characteristics of aerosol particles at the King Sejong Station, Antarctic Peninsula, *Atmos.*
827 *Chem. Phys.*, 17, 12985–12999, <https://doi.org/10.5194/acp-17-12985-2017>, 2017.
- 828 Kim, J., Yoon, Y. J., Gim, Y., Choi, J. H., Kang, H. J., Park, K.-T., Park, J., and Lee, B. Y.: New particle
829 formation events observed at King Sejong Station, Antarctic Peninsula – Part 1: Physical
830 characteristics and contribution to cloud condensation nuclei, *Atmos. Chem. Phys.*, 19, 7583–7594,
831 <https://doi.org/10.5194/acp-19-7583-2019>, 2019.
- 832 Kim, J. H., Ahn, I. -Y., Lee, K. S., Chung, H., and Choi, H.-G.: Vegetation of Barton Peninsula in the
833 neighbourhood of King Sejong Station (King George Island, maritime Antarctic), *Polar, Biol.*, 30,
834 903–916, <https://doi.org/10.1007/s00300-006-0250-2>, 2007.
- 835 Komppula, M., Lihavainen, H., Kerminen, V.-M., Kulmala, M., and Viisanen, Y.: Measurements of cloud
836 droplet activation of aerosol particles at a clean subarctic background site, *J. Geophys. Res.*, 110,
837 D06204, [doi:10.1029/2004JD005200](https://doi.org/10.1029/2004JD005200), 2005.
- 838 Kulmala, M., Vehkamäki, H., Petäjä, T., Dal Maso, M., Lauri, A., Kerminen, V. M., Birmili, W., and
839 McMurry, P. H.: Formation and growth rates of ultrafine atmospheric particles: a review of
840 observations, *J. Aerosol Sci.*, 35, 143–176, <https://doi.org/10.1016/j.jaerosci.2003.10.003>, 2004.
- 841 Kulmala, M., Petäjä, T., Nieminen, T., Sipilä, M., Manninen, H. E., Lehtipalo, K., Dal Maso, M., Aalto,
842 P. P., Junninen, H., Paasonen, P., Riipinen, I., Lehtinen, K. E. J., Laaksonen, A., and Kerminen, V.-
843 M.: Measurement of the nucleation of atmospheric aerosol particles, *Nat. Protoc.*, 7, 1651–1667,
844 2012.
- 845 Kulmala, M., Kontkanen, J., Junninen, H., Lehtipalo, K., Manninen, H. E. Nieminen, T., Petäjä, T., Sipilä,
846 M., Schobesberger, S., Rantala, P., Franchin, A., Jokinen, T., Järvinen, E., Äijälä, M., Kangasluoma,
847 J., Hakala, J., Aalto, P. P., Paasonen, P., Mikkilä, J., Vanhanen, J., Aalto, J., Hakola, H., Makkonen,
848 U., Ruuskanen, T., Mauldin III, R. L., Duplissy, J., Vehkamäki, H., Bäck, J., Kortelainen, A.,
849 Riipinen, I., Kurtén, T., Johnston, M. V., Smith,
850 Kyrö, E.-M., Kerminen, V.-M., Virkkula, A., Dal Maso, M., Parshintsev, J., Ruíz-Jimenez, J., Forsström,
851 L., Manninen, H. E., Riekkola, M.-L., Heinonen, P., and Kulmala, M.: Antarctic new particle
852 formation from continental biogenic precursors, *Atmos. Chem. Phys.*, 13, 3527–3546,
853 <https://doi.org/10.5194/acp-13-3527-2013>, 2013.
- 854 Laaksonen, A., Kulmala, M., O’Dowd, C. D., Joutsensaari, J., Vaattovaara, P., Mikkonen, S., Lehtinen,
855 K. E. J., Sogacheva, L., Dal Maso, M., Aalto, P., Petäjä, T., Sogachev, A., Yoon, Y. J., Lihavainen,
856 H., Nilsson, D., Facchini, M. C., Cavalli, F., Fuzzi, S., Hoffmann, T., Arnold, F., Hanke, M., Sellegri,
857 K., Umann, B., Junkermann, W., Coe, H., Allan, J. D., Alfarra, M. R., Worsnop, D. R., Riekkola,
858 M.-L., Hyötyläinen, T., and Viisanen, Y.: The role of VOC oxidation products in continental new
859 particle formation, *Atmos. Chem. Phys.*, 8, 2657–2665, <https://doi.org/10.5194/acp-8-2657-2008>,
860 2008.
- 861 Lachlan-Cope, T., Beddows, D. C. S., Brough, N., Jones, A. E., Harrison, R. M., Lupi, A., Yoon, Y. J.,
862 Virkkula, A., and Dall’Osto, M.: On the annual variability of Antarctic aerosol size distributions at
863 Halley Research Station, *Atmos. Chem. Phys.*, 20, 4461–4476, <https://doi.org/10.5194/acp-20-4461-2020>, 2020.
- 865 Lange, B. A., Katlein, C., Castellani, G., Fernández-Méndez, M., Nicolaus, M., Peeken, I., and Flores, H.:
866 Characterizing spatial variability of ice algal chlorophyll a and net primary production between sea
867 ice habitats using horizontal profiling platforms, *Front. in Mar. Sci.*, 4, 349, 2017.
- 868 Lee, Y.J., Matrai, P.A., Friedrichs, M.A., Saba, V.S., Antoine, D., Ardyna, M., Asanuma, I., Babin, M.,

- 869 [Béanger, S., and Benoît-Gagné, M.: An assessment of phytoplankton primary productivity in the](#)
870 [Arctic Ocean from satellite ocean color/in situ chlorophyll-a based models, *J. Geophys. Res.*, 120,](#)
871 [6508–6541, doi: 10.1002/2015JC011018, 2015.](#)
- 872 Lee, Y. I., Lim, H. S., and Yoon, H. I.: Carbon and nitrogen isotope composition of vegetation on King
873 George Island, maritime Antarctic, *Polar Biol.* 32, 1607–1615). [https://doi.org/10.1007/s00300-](https://doi.org/10.1007/s00300-009-0659-5)
874 [009-0659-5](https://doi.org/10.1007/s00300-009-0659-5), 2009.
- 875 Legrand, M., Ducroz, F., Wagenbach, D., Mulvaney, R., and Hall, J.: Ammonium in coastal Antarctic
876 aerosol and snow: Role of polar ocean and penguin emissions, *J. Geophys. Res.*, 103, 11043–11056,
877 1998.
- 878 Liu, J., Dedrick, J., Russell, L. M., Senum, G. I., Uin, J., Kuang, C., Springston, S. R., Leaitch, W. R.,
879 Aiken, A. C., and Lubin, D.: High summertime aerosol organic functional group concentrations
880 from marine and seabird sources at Ross Island, Antarctica, during AWARE, *Atmos. Chem. Phys.*,
881 18, 8571–8587, <https://doi.org/10.5194/acp-18-8571-2018>, 2018.
- 882 Miranda, V., Pina, P., Heleno, S., Vieira, G., Mora, C., and Schaefer, C.E.: Monitoring recent changes of
883 vegetation in Fildes Peninsula (King George Island, Antarctica) through satellite imagery guided by
884 UAV surveys. *Sci. Total Environ.* 704, 135295. <https://doi.org/10.1016/j.scitotenv.2019.135295>,
885 2020.
- 886 O’Dowd, C. D.: On the spatial extent and evolution of coastal aerosol plumes, *J. Geophys. Res.-Atmos.*,
887 107, 8105, doi:10.1029/2001JD000422, 2002
- 888 O’Dowd, C. D., Lowe, J. A., Smith, M. H., Davison, B., Hewitt, C. N., and Harrison, R. M.: Biogenic
889 sulphur emissions and inferred non-sea-salt-sulphate cloud condensation nuclei in and around
890 Antarctica, *J. Geophys. Res.-Atmos.* 102, 12839–12854, 1997.
- 891 Pant, V., Singh, D., and Kamra, A. K.: Size distribution of atmospheric aerosols at Maitri, Antarctica,
892 *Atmos. Environ.*, 45, 5138–5149, 2011.
- 893 Park, J., Dall’Osto, M., Park, K., Gim, Y., Kang, H. J., Jang, E., Park, K.-T., Park, M., Yum, S. S., Jung,
894 J., Lee, B. Y., and Yoon, Y. J.: Shipborne observations reveal contrasting Arctic marine, Arctic
895 terrestrial and Pacific marine aerosol properties, *Atmos. Chem. Phys.*, 20, 5573–5590,
896 <https://doi.org/10.5194/acp-20-5573-2020>, 2020.
- 897 Park, J., Sakurai, H., Vollmers, K., and McMurry, P. H.: Aerosol size distributions measured at South Pole
898 during ISCAT, *Atmos. Environ.*, 38, 5493–5500, doi:10.1016/j.atmosenv.2002.12.001, 2004.
- 899 Park, K. T., Lee, K., Kim, T. W., Yoon, Y. J., Jang, E. H., Jang, S., Lee, B. Y. and Hermansen, O.:
900 Atmospheric DMS in the Arctic Ocean and its relation to phytoplankton biomass, *Global*
901 *Biogeochem. Cy.*, 32, 351–359, <https://doi.org/10.1002/2017GB005805>, 2018.
- 902 Park, K.-T., Yoon, Y.J., Lee, K., Tunved, P., Krejci, R., Ström, J., Jang, E., Kang, H.J., Jang, S., Park, J.,
903 Lee, B.Y., Traversi, R., Becagli, S., and Hermansen, O.: Dimethyl Sulfide-Induced Increase in
904 Cloud Condensation Nuclei in the Arctic Atmosphere, *Global Biogeochem. Cy.*, 35,
905 e2021GB006969, <https://doi.org/10.1029/2021GB006969>, 2021.
- 906 Parkinson, C. L. and Cavalieri, D. J.: Antarctic sea ice variability and trends, 1979–2010, *The Cryosphere*,
907 6, 871–880, <https://doi.org/10.5194/tc-6-871-2012>, 2012.
- 908 Pritchard, H. D., Arthern, R. J., Vaughan, D. G., and Edwards, L. A.: Extensive dynamic thinning on the
909 margins of the Greenland and Antarctic ice sheets, *Nature*, 461, 971–975, 2009.
- 910 Pushpawela, B., Jayaratne, R., and Morawska, L.: The influence of wind speed on new particle formation
911 events in an urban environment, *Atmos. Res.* 215, 37–41, 2019.
- 912 Quéléver, L. L. J., Dada, L., Asmi, E., Lampilahti, J., Chan, T., Ferrara, J. E., Copes, G. E., Pérez-Fogwill,
913 G., Barreira, L., Aurela, M., Worsnop, D. R., Jokinen, T., and Sipilä, M.: Investigation of new
914 particle formation mechanisms and aerosol processes at Marambio Station, Antarctic Peninsula,
915 *Atmos. Chem. Phys.*, 22, 8417–8437, <https://doi.org/10.5194/acp-22-8417-2022>, 2022.
- 916 Roscoe, H. K., Jones, A. E., Brough, N., Weller, R., Saiz-Lopez, A., Mahajan, A. S., Schoenhardt, A.,
917 Burrows, J.P., and Fleming, Z. L.: Particles and iodine compounds in coastal Antarctica, *J. Geophys.*
918 *Res.-Atmos.*, 120, 7144–7156, <https://doi.org/10.1002/2015JD023301>, 2015.
- 919 Saiz-Lopez, A., Mahajan, A. S., Salmon, R. A., Bauguitte, S. J. B., Jones, A. E., Roscoe, H. K., and Plane,

- 920 J. M. C.: Boundary layer halogens in coastal Antarctica, *Science*, 317, 348–351,
921 doi:10.1126/science.1141408, 2007.
- 922 Schmale, J., Baccarini, A., Thurnherr, I., Henning, S., Efraim, A., Regayre, L., Bolas, C., Hartmann, M.,
923 Welti, A., Lehtipalo, K., Aemisegger, F., Tatzelt, C., Landwehr, S., Modini, R. L., Tummon, F.,
924 Johnson, J., Harris, N., Schnaiter, M., Toffoli, A., Derkani, M., Bukowiecki, N., Stratmann, F.,
925 Dommen, J., Baltensperger, U., Wernli, H., Rosenfeld, D., Gysel-Beer, M., and Carslaw, K.:
926 Overview of the Antarctic Circumnavigation Expedition: Study of Preindustrial-like Aerosols and
927 Their Climate Effects (ACE-SPACE), *B. Am. Meteorol. Soc.*, 100, 2260–2283,
928 <https://doi.org/10.1175/BAMS-D-18-0187.1>, 2019.
- 929 Schmale, J., Schneider, J., Nemitz, E., Tang, Y. S., Dragosits, U., Blackall, T. D., Trathan, P. N., Phillips,
930 G. J., Sutton, M., and Braban, C. F.: Sub-Antarctic marine aerosol: dominant contributions from
931 biogenic sources, *Atmos. Chem. Phys.*, 13, 8669–8694, <https://doi.org/10.5194/acp-13-8669-2013>,
932 2013.
- 933 Schönhardt, A., Richter, A., Wittrock, F., Kirk, H., Oetjen, H., Roscoe, H. K., and Burrows, J. P.:
934 Observations of iodine monoxide columns from satellite, *Atmos. Chem. Phys.*, 8, 637–653,
935 doi:10.5194/acp-8-637-2008, 2008.
- 936 Simó, R.: Production of atmospheric sulfur by oceanic plankton: biogeochemical, ecological and
937 evolutionary links: *Trends. Ecol. Evol.*, 16, 287–294, [https://doi.org/10.1016/S0169-5347\(01\)02152-8](https://doi.org/10.1016/S0169-5347(01)02152-8), 2001.
- 939 Simmons, J. B., Humphries, R. S., Wilson, S. R., Chambers, S. D., Williams, A. G., Griffiths, A. D.,
940 McRobert, I. M., Ward, J. P., Keywood, M. D., and Gribben, S.: Summer aerosol measurements
941 over the East Antarctic seasonal ice zone, *Atmos. Chem. Phys.*, 21, 9497–9513,
942 <https://doi.org/10.5194/acp-21-9497-2021>, 2021.
- 943 Sipilä, M., Sarnela, N., Jokinen, T., Henschel, H., Junninen, H., Kontkanen, J., Richters, S., Kangasluoma,
944 J., Franchin, A., Peräkylä, O., Rissanen, M. P., Ehn, M., Vehkamäki, H., Kurten, T., Berndt, T.,
945 Petäjä, T., Worsnop, D., Ceburnis, D., Kerminen, V. M., Kulmala, M., and O'Dowd, C.: Molecular-
946 scale evidence of aerosol particle formation via sequential addition of HIO₃, *Nature*, 537, 532–534,
947 <https://doi.org/10.1038/nature19314>, 2016.
- 948 Stroeve, J. C., Jenouvrier, S., Campbell, G. G., Barbraud, C., and Delord, K.: Mapping and assessing
949 variability in the Antarctic marginal ice zone, pack ice and coastal polynyas in two sea ice
950 algorithms with implications on breeding success of snow petrels, *The Cryosphere*, 10, 1823–1843,
951 <https://doi.org/10.5194/tc-10-1823-2016>, 2016.
- 952 Ström, J., Engvall, A. C., Delbart, F., Krejci, R., and Treffeisen, R.: On small particles in the Arctic
953 summer boundary layer: observations at two different heights near Ny-Ålesund, Svalbard, *Tellus B*,
954 61, 473–482, 2009.
- 955 Suni, T., Kulmala, M., Hirsikko, A., Bergman, T., Laakso, L., Aalto, P. P., Leuning, R., Cleugh, H., Zegelin,
956 S., Hughes, D., van Gorsel, E., Kitchen, M., Vana, M., Hörrak, U., Mirme, S., Mirme, A., Sevanto,
957 S., Twining, J., and Tadros, C.: Formation and characteristics of ions and charged aerosol particles
958 in a native Australian Eucalypt forest, *Atmos. Chem. Phys.*, 8, 129–139,
959 <https://doi.org/10.5194/acp-8-129-2008>, 2008.
- 960 Svenningsson, B., Arneth, A., Hayward, S., Holst, T., Massling, A., Swietlicki, E., Hirsikko, A., Junninen,
961 H., Riipinen, I., Vana, M., Maso, M. D., Hussein, T., and Kulmala, M.: Aerosol particle formation
962 events and analysis of high growth rates observed above a subarctic wetland–forest mosaic, *Tellus*
963 *B: Chem. Phys. Meteorol.*, 60, 353–364, <https://doi.org/10.1111/j.1600-0889.2008.00351.x>, 2008.
- 964 Teinilä, K., Frey, A., Hillamo, R., Tülp, H. C., and Weller, R.: A study of the sea-salt chemistry using size-
965 segregated aerosol measurements at coastal Antarctic station Neumayer, *Atmos. Environ.*, 96, 11–
966 19, 2014.
- 967 Tremblay, S., Picard, J.-C., Bachelder, J. O., Lutsch, E., Strong, K., Fogal, P., Leitch, W. R., Sharma, S.,
968 Kolonjari, F., Cox, C. J., Chang, R. Y.-W., and Hayes, P. L.: Characterization of aerosol growth
969 events over Ellesmere Island during the summers of 2015 and 2016, *Atmos. Chem. Phys.*, 19, 5589–

5604, <https://doi.org/10.5194/acp-19-5589-2019>, 2019.

- Vaughan, D. G., Marshall, G. J., Connolley, W. M., Parkinson, C., Mulvaney, R., Hodgson, D. A., King, J. C., Pudsey, C. J., and Turner, J.: Recent rapid regional climate warming on the Antarctic Peninsula, *Climatic Change*, 60, 243–274, <https://doi.org/10.1023/a:1026021217991>, 2003.
- Vehkamäki, H., Dal Maso, M., Hussein, T., Flanagan, R., Hyvärinen, A., Lauros, J., Merikanto, P., Mönkkönen, M., Pihlatie, K., Salminen, K., Sogacheva, L., Thum, T., Ruuskanen, T. M., Keronen, P., Aalto, P. P., Hari, P., Lehtinen, K. E. J., Rannik, Ü., and Kulmala, M.: Atmospheric particle formation events at Värriö measurement station in Finnish Lapland 1998–2002, *Atmos. Chem. Phys.*, 4, 2015–2023, <https://doi.org/10.5194/acp-4-2015-2004>, 2004.
- Virkkula, A., Teinilä, K., Hillamo, R., Kerminen, V.-M., Saarikoski, S., Aurela, M., Viidanoja, J., Paatero, J., Koponen, I. K., Kulmala, M.: Chemical composition of boundary layer aerosol over the Atlantic Ocean and at an Antarctic site, *Atmos. Chem. Phys.*, 6, 3407–3421, 2006.
- Virkkula, A., Hirsikko, A., Vana, M., Aalto, P. P., Hillamo, R., and Kulmala, M.: Charged particle size distributions and analysis of particle formation events at the Finnish Antarctic research station Aboa, *Boreal Environ. Res.*, 12, 397–408, 2007.
- Walton, D. W. H. and Thomas, J.: Cruise Report – Antarctic Circumnavigation Expedition (ACE) 20th December 2016 – 19th March 2017, Tech. rep., Zenodo, <https://doi.org/10.5281/zenodo.1443511>, 2018.
- Weber, R. J., Marti, J. J., McMurry, P. H., Eisele, F. L., Tanner, D. J., and Jefferson, A.: Measurements of new particle formation and ultrafine particle growth rates at a clean continental site, *J. Geophys. Res.*, 102, 4375–4385, 1997.
- Weber, R. J., McMurry, P. H., Mauldin, L., Tanner, D. J., Eisele, F. L., Brechtel, F. J., Kreidenweis, S. M., Kok, G. L., Schillawski, R. D., and Baumgardner, D.: A study of new particle formation and growth involving biogenic and trace gas species measured during ACE 1, *J. Geophys. Res.-Atmos.*, 103, 16385–16396, <https://doi.org/10.1029/97jd02465>, 1998.
- Weller, R., Minikin, A., Wagenbach, D., and Dreiling, V.: Characterization of the inter-annual, seasonal, and diurnal variations of condensation particle concentrations at Neumayer, Antarctica, *Atmos. Chem. Phys.*, 11, 13243–13257, <https://doi.org/10.5194/acp-11-13243-2011>, 2011.
- Weller, R., Schmidt, K., Teinilä, K., and Hillamo, R.: Natural new particle formation at the coastal Antarctic site Neumayer, *Atmos. Chem. Phys.*, 15, 11399–11410, <https://doi.org/10.5194/acp-15-11399-2015>, 2015.
- Weller, R., Legrand, M., and Preunkert, S.: Size distribution and ionic composition of marine summer aerosol at the continental Antarctic site Kohnen, *Atmos. Chem. Phys.*, 18, 2413–2430, <https://doi.org/10.5194/acp-18-2413-2018>, 2018.
- Williamson, C. J., Kupc, A., Axisa, A., Kelsey R., Bilsback, K. R, Bui, T. P., Campuzano-Jost, P., Dollner, M., Froyd, K. D., Hodshire, A. L., Jimenez, J. L., Kodros, J. K., Luo, G., Murphy, D. M., Nault, B. A., Ray, E. A., Weinzierl, B., Wilson, J. C., Yu, F., Yu, P., Pierce, J. R., and Brock, C. A.: A large source of cloud condensation nuclei from new particle formation in the tropics, *Nature*, 574, 399–403, <https://doi.org/10.1038/s41586-019-1638-9>, 2019.
- Willis, M. D., Burkart, J., Thomas, J. L., Köllner, F., Schneider, J., Bozem, H., Hoor, P. M., Aliabadi, A. A., Schulz, H., Herber, A. B., Leitch, W. R., and Abbatt, J. P. D.: Growth of nucleation mode particles in the summertime Arctic: a case study, *Atmos. Chem. Phys.*, 16, 7663–7679, <https://doi.org/10.5194/acp-16-7663-2016>, 2016.
- Yli-Juuti, T., Riipinen, I., Aalto, P. P., Nieminen, T., Maenhaut, W., Janssens, I. A., Claeys, M., Salma, I., Ocskay, R., Hoffer, A., Imre, K., and Kulmala, M.: Characteristics of new particle formation events and cluster ions at K-pusztá, Hungary, *Boreal Environ. Res.*, 14, 683–698, 2009.
- Yu, F. and Luo, G.: Oceanic dimethyl sulfide emission and new particle formation around the coast of Antarctica: a modeling study of seasonal variations and comparison with measurements, *Atmosphere*, 1, 34–50, 2010
- Zheng, G., Wang, Y., Wood, R., Jensen, M. P., Kuang, C., McCoy, I. L., Matthews, A., Mei, F., Tomlinson, J. M., Shilling, J. E., Zawadowicz, M. A., Crosbie, E., Moore, R., Ziemba, L., Andreae, M. O., and

1021 Wang, J.: New particle formation in the remote marine boundary layer. *Nat Commun.* 12(1), 527.
1022 doi: 10.1038/s41467-020-20773-1, 2021.

1023 Zhu, R. B., Sun, J. J., Liu, Y. S., Gong, Z. J., and Sun, L. G.: Potential ammonia emissions from penguin
1024 guano, ornithogenic soils and seal colony soils in coastal Antarctica: effects of freezing thawing
1025 cycles and selected environmental variables, *Antarct. Sci.*, 23, 78–92,
1026 doi:10.1017/s0954102010000623, 2011.

Table 1. Monthly median for total particle number concentration > 10 nm (CN_{10}), particle number concentrations of the nucleation mode (N_{NUC}), Aitken mode (N_{AIT}), accumulation mode (N_{ACC}), CCN number concentration at supersaturation of 0.4% ($CCN_{0.4\%}$), and meteorological parameters such as solar radiation, temperature, RH, pressure, wind speed, and wind direction for 2018, after data filtering ($BC < 50$ ng m^{-3} indicating pristine and clean conditions), measured at King Sejong Station in the Antarctic Peninsula from January 1 to December 31, 2018.

| | CN_{10} (cm^{-3}) | N_{NUC}^a (cm^{-3}) | N_{AIT}^a (cm^{-3}) | N_{ACC}^a (cm^{-3}) | $CCN_{0.4\%}$ (cm^{-3}) | Solar radiation ($W\ m^{-2}$) | Temp. ($^{\circ}C$) | RH (%) | Pressure (hPa) | Wind Speed ($m\ s^{-1}$) | Wind direction ($^{\circ}$) |
|-----------|----------------------------|------------------------------|------------------------------|------------------------------|--------------------------------|---------------------------------------|--------------------------|-----------|-------------------|----------------------------------|-------------------------------------|
| January | 506.2 | 101.1 | 188.7 | 83.8 | 235.2 | 129.2 | 1.1 | 88.6 | 986.0 | 5.78 | 315.8 |
| February | 594.3 | 111.3 | 200.0 | 69.9 | 229.8 | 103.5 | 1.8 | 90.8 | 987.2 | 7.72 | 319.9 |
| March | 357.3 | 86.0 | 112.4 | 42.1 | 138.7 | 58.0 | 1.1 | 88.4 | 981.8 | 8.21 | 342.3 |
| April | 184.1 | 49.9 | 39.1 | 17.5 | 58.6 | 26.2 | -0.7 | 87.1 | 988.2 | 7.88 | 350.0 |
| May | 106.7 | 25.1 | 23.8 | 14.2 | 51.1 | 7.3 | -2.3 | 81.8 | 990.1 | 7.34 | 277.7 |
| June | 75.9 | 12.2 | 12.5 | 9.2 | 35.4 | 3.4 | -4.1 | 88.4 | 995.9 | 7.21 | 339.8 |
| July | 84.3 | 28.2 | 16.8 | 11.6 | 39.1 | 5.5 | -2.9 | 86.5 | 992.2 | 9.08 | 300.8 |
| August | 109.8 | 39.3 | 19.6 | 14.8 | 52.1 | 21.8 | -3.3 | 85.9 | 986.2 | 8.57 | 327.8 |
| September | 266.4 | 123.8 | 51.3 | 20.9 | 79.3 | 65.6 | -3.6 | 86.5 | 992.6 | 9.52 | 313.2 |
| October | 287.0 | 88.9 | 62.0 | 26.9 | 105.3 | 122.1 | -2.1 | 84.6 | 994.4 | 6.50 | 290.8 |
| November | 498.2 | 79.3 | 136.8 | 46.1 | 150.3 | 143.3 | -0.6 | 89.3 | 980.0 | 7.59 | 307.9 |
| December | 511.9 | 193.5 | 227.6 | 67.7 | 189.1 | 136.5 | 0.4 | 87.2 | 980.4 | 6.72 | 302.7 |

^a N_{NUC} , N_{AIT} , and N_{ACC} represent the particle number concentrations in the nucleation mode (2.5–25 nm), Aitken mode (25–100 nm), and accumulation mode (100–300 nm).

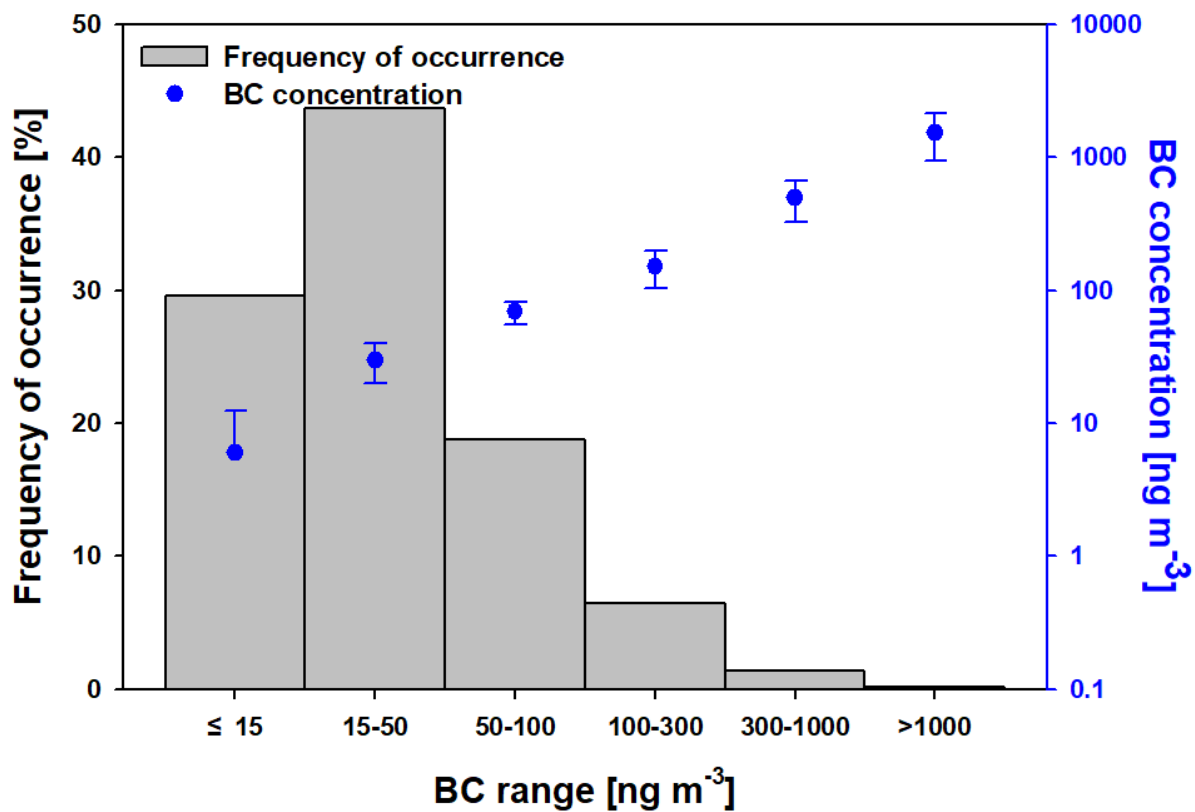


Figure 1. Frequency of occurrence of BC mass concentration for six types of Antarctic Peninsula air-pollution levels classified from four-year BC data.

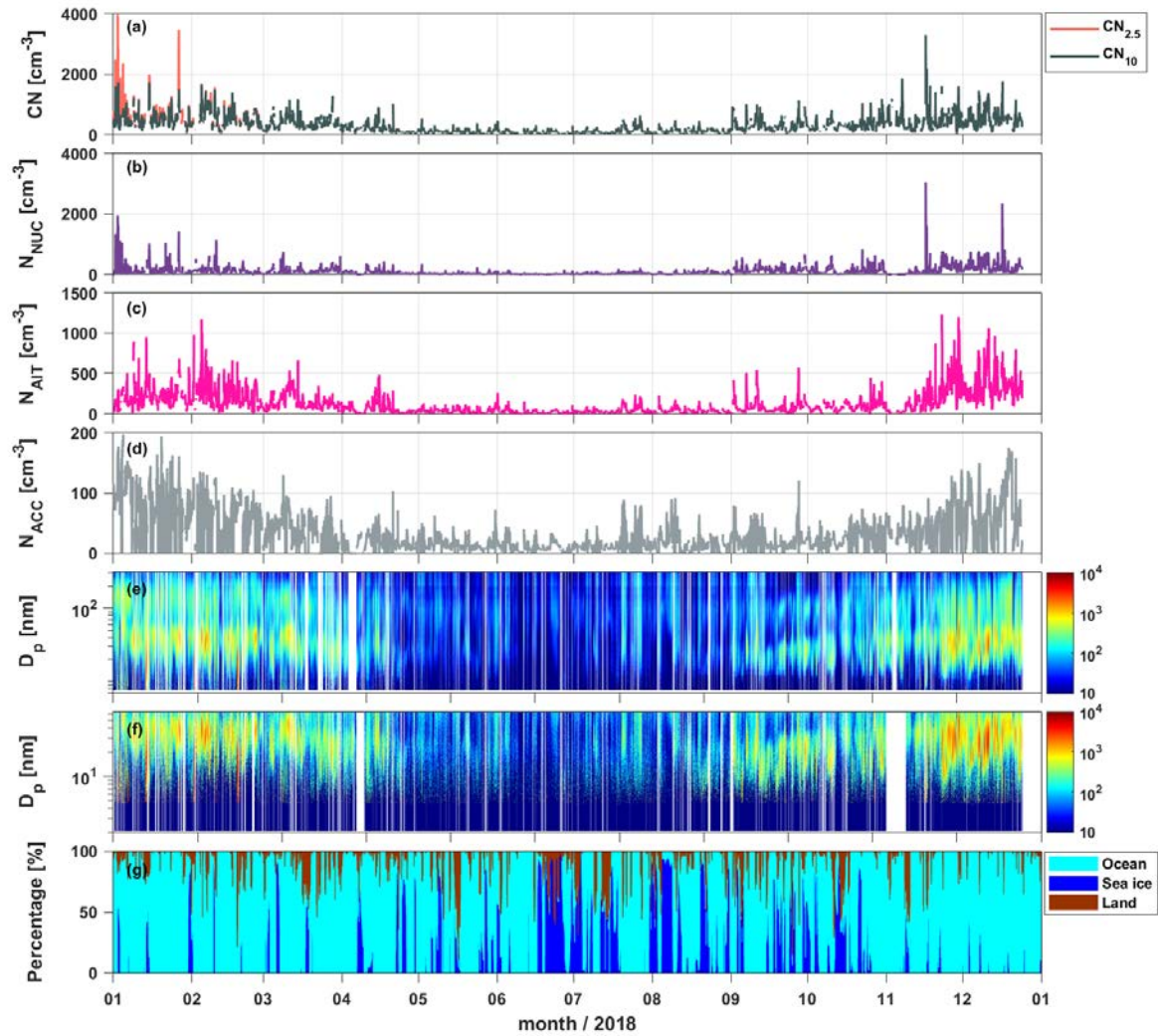


Figure 2. Time series of 1 h averages for (a) $CN_{2.5}$ and CN_{10} , (b) nucleation mode (N_{NUC} ; 2.5–25 nm), (c) Aitken mode (N_{AIT} ; 25–100 nm), and (d) accumulation mode (N_{ACC} ; 100–300 nm); contour plots of the size distributions measured using (e) standard and (f) nano-SMPS; and (g) residence time of air masses passing over ocean, sea ice, and land. $CN_{2.5}$ data are only available from January to March due to the instrumental malfunctions.

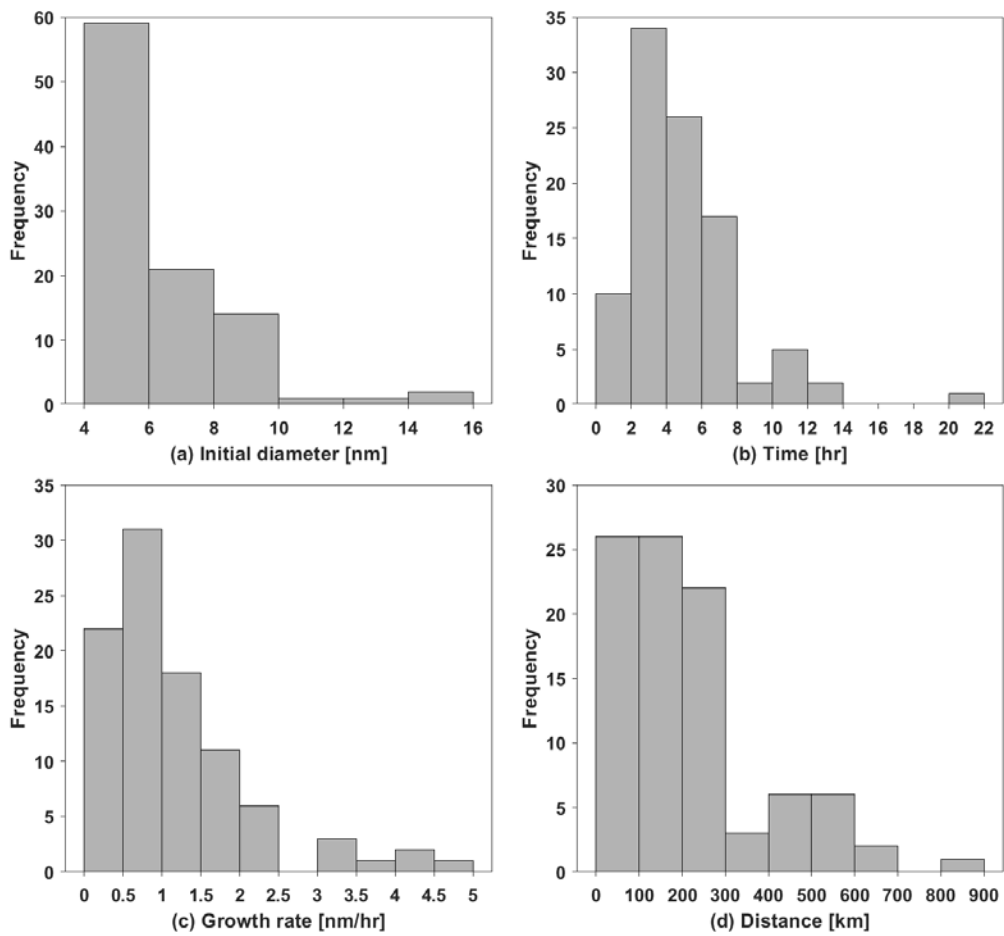


Figure 3. Frequency of (a) initial diameter of particles, (b) duration time, (c) growth rate, and (d) extension for the NPF event. Two NPF cases were excluded when the wind speed was higher than 10 ms^{-1} .

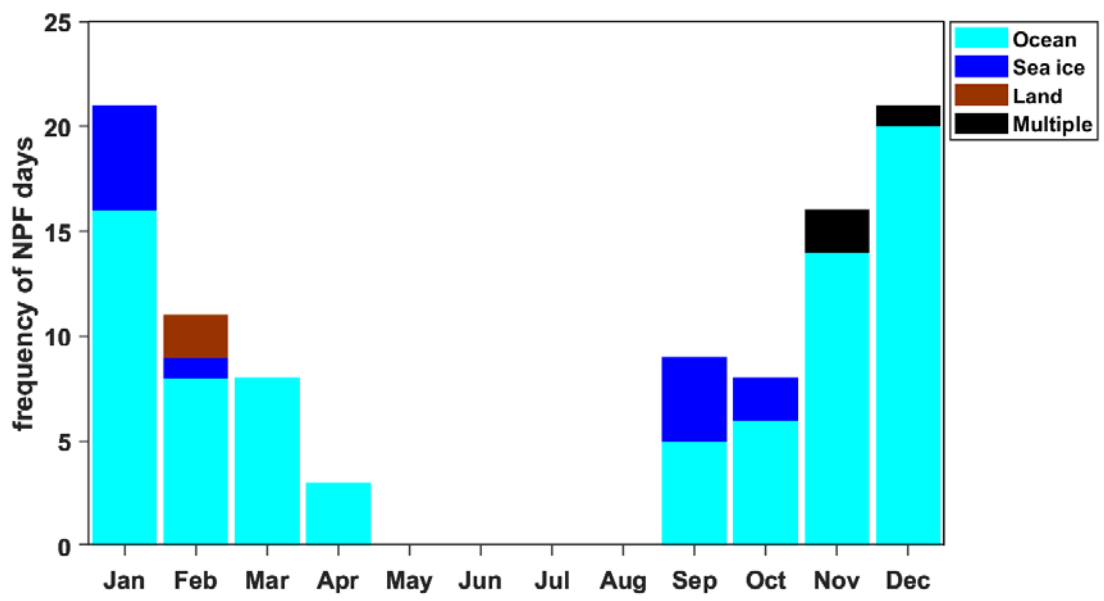


Figure 4. Seasonal variations in the number of NPF days by air mass origin.

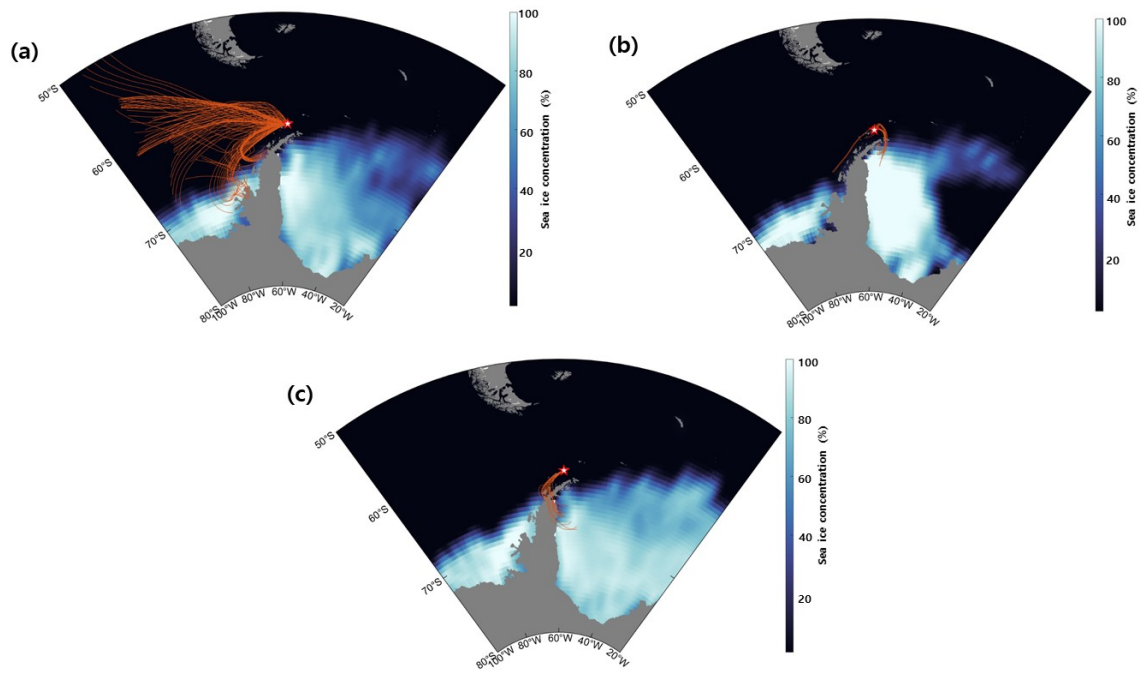


Figure 5. Air mass back trajectories for arrival at 50 m for the three case study NPF events: (a) marine, (b) sea ice, and (c) multiple.

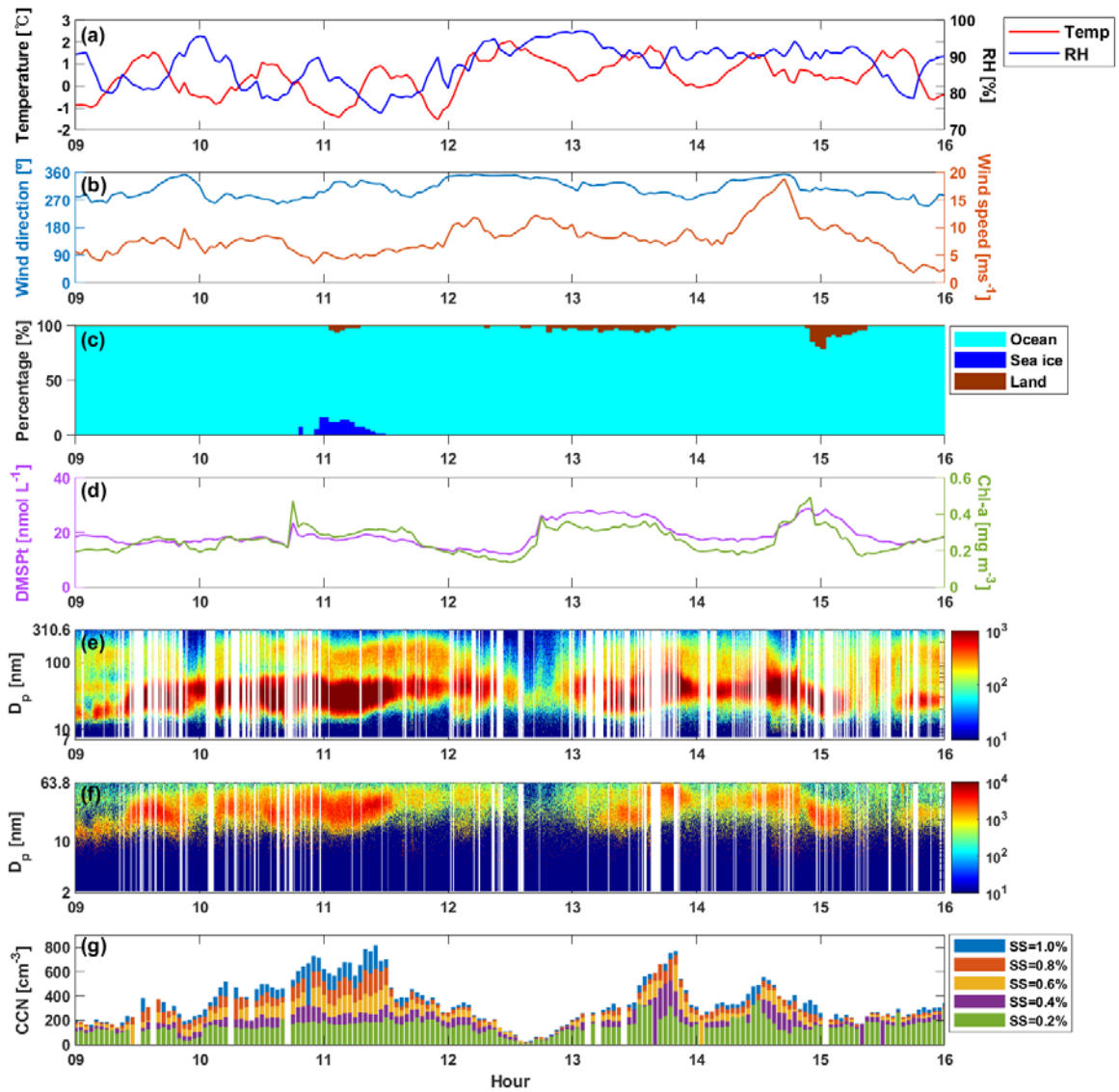


Figure 6. Marine NPF event observed from December 9–15, 2018. (a–b) meteorological variables, (c) the residence time of air masses that passed over the ocean, sea ice and land areas, (d) total DMSP and chlorophyll exposures, (e–f) number size distribution with the standard-SMPS and nano-SMPS, and (g) CCN number concentration. The x-axis represents local time.

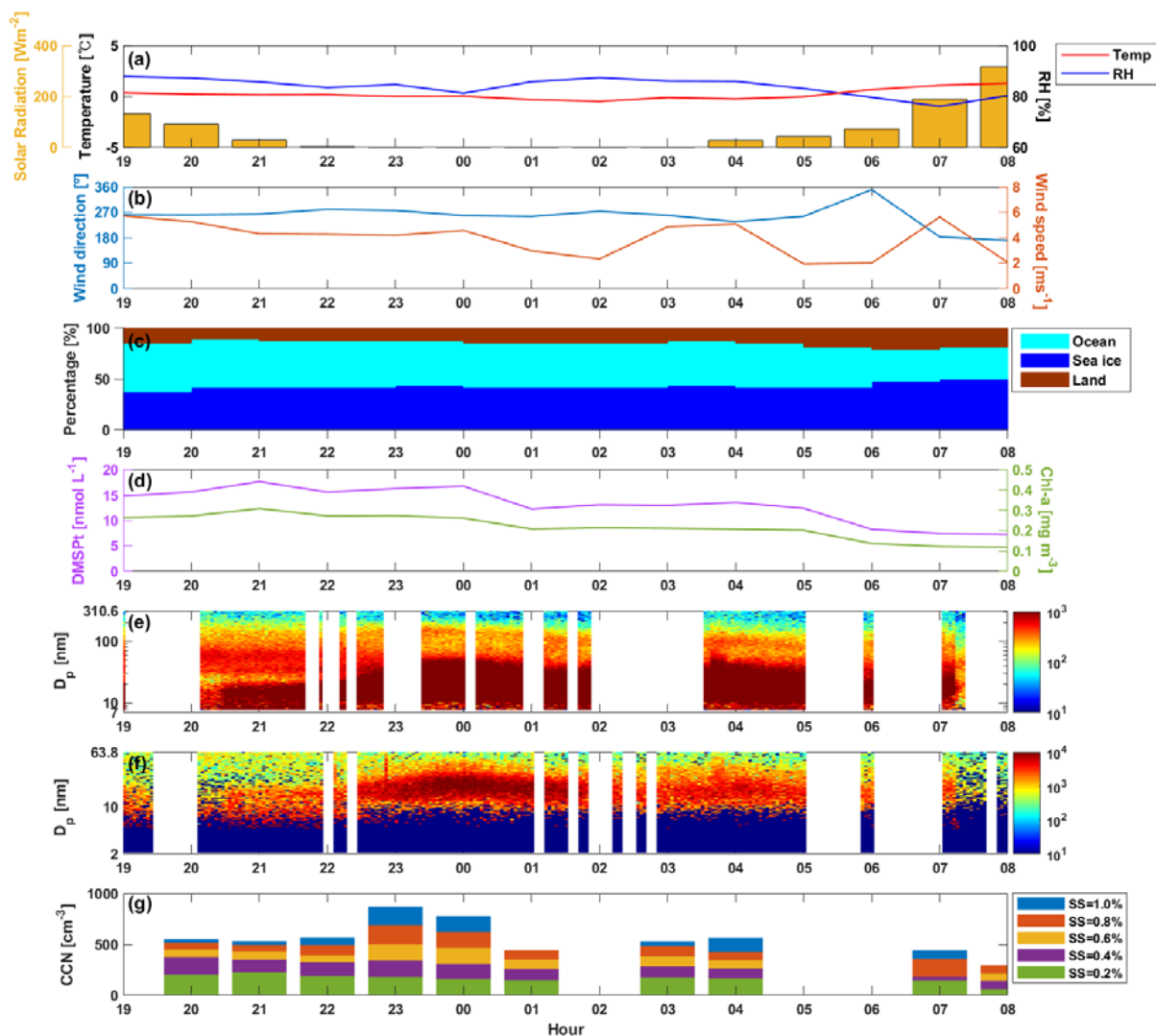


Figure 7. Sea ice NPF event observed from January 13–14, 2018. (a–b) meteorological variables, (c) the residence time of air masses that passed over the ocean, sea ice and land areas, (d) total DMSP and chlorophyll exposures, (e–f) number size distribution with the standard-SMPS and nano-SMPS, and (g) CCN number concentration. The x-axis represents local time.

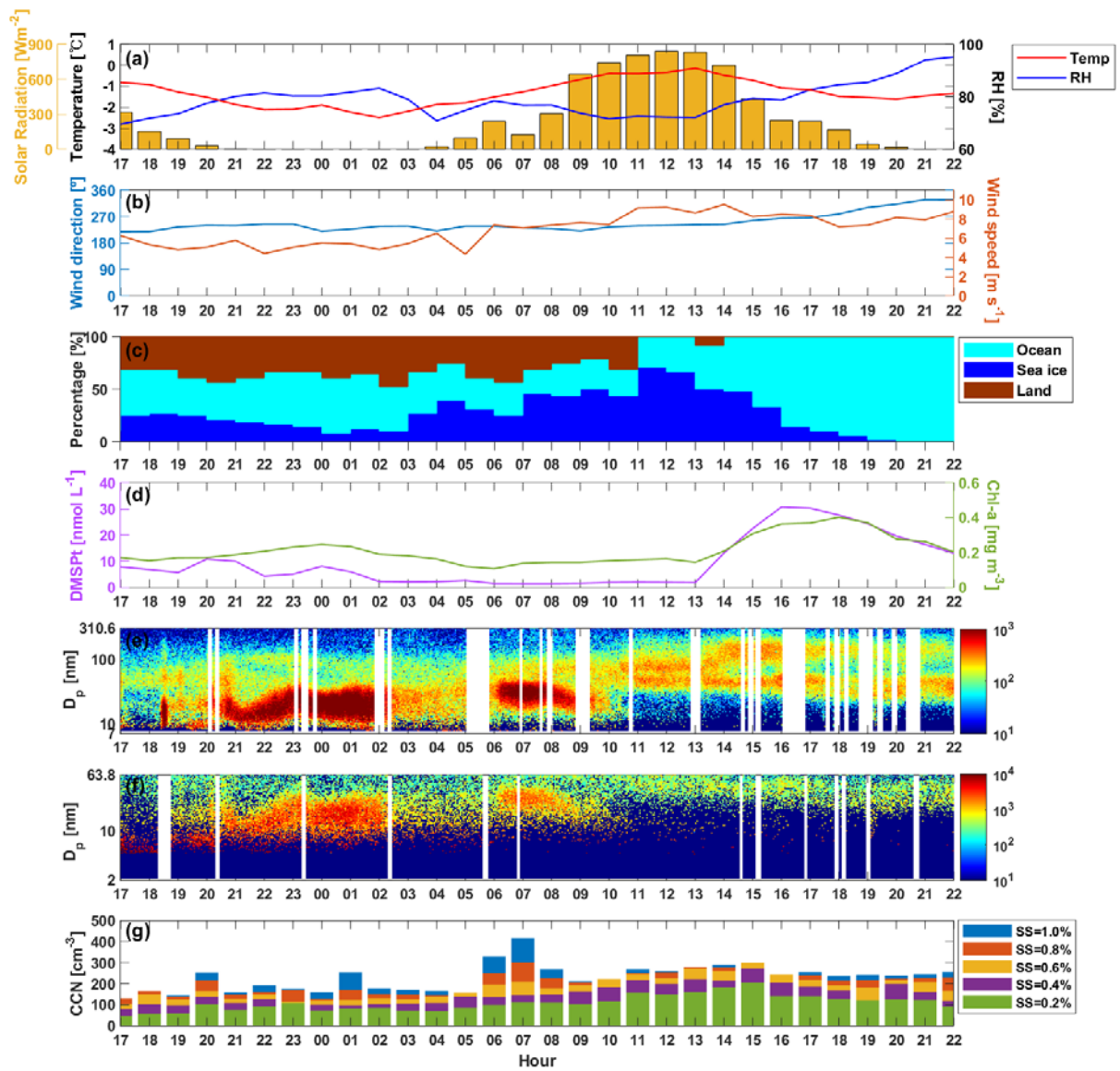


Figure 8. Multiple NPF event observed from November 16–17, 2018. (a–b) meteorological variables, (c) the residence time of air masses that passed over the ocean, sea ice and land areas, (d) total DMSP and chlorophyll exposures, (e–f) number size distribution with the standard-SMPS and nano-SMPS, and (g) CCN number concentration. The x-axis represents local time.

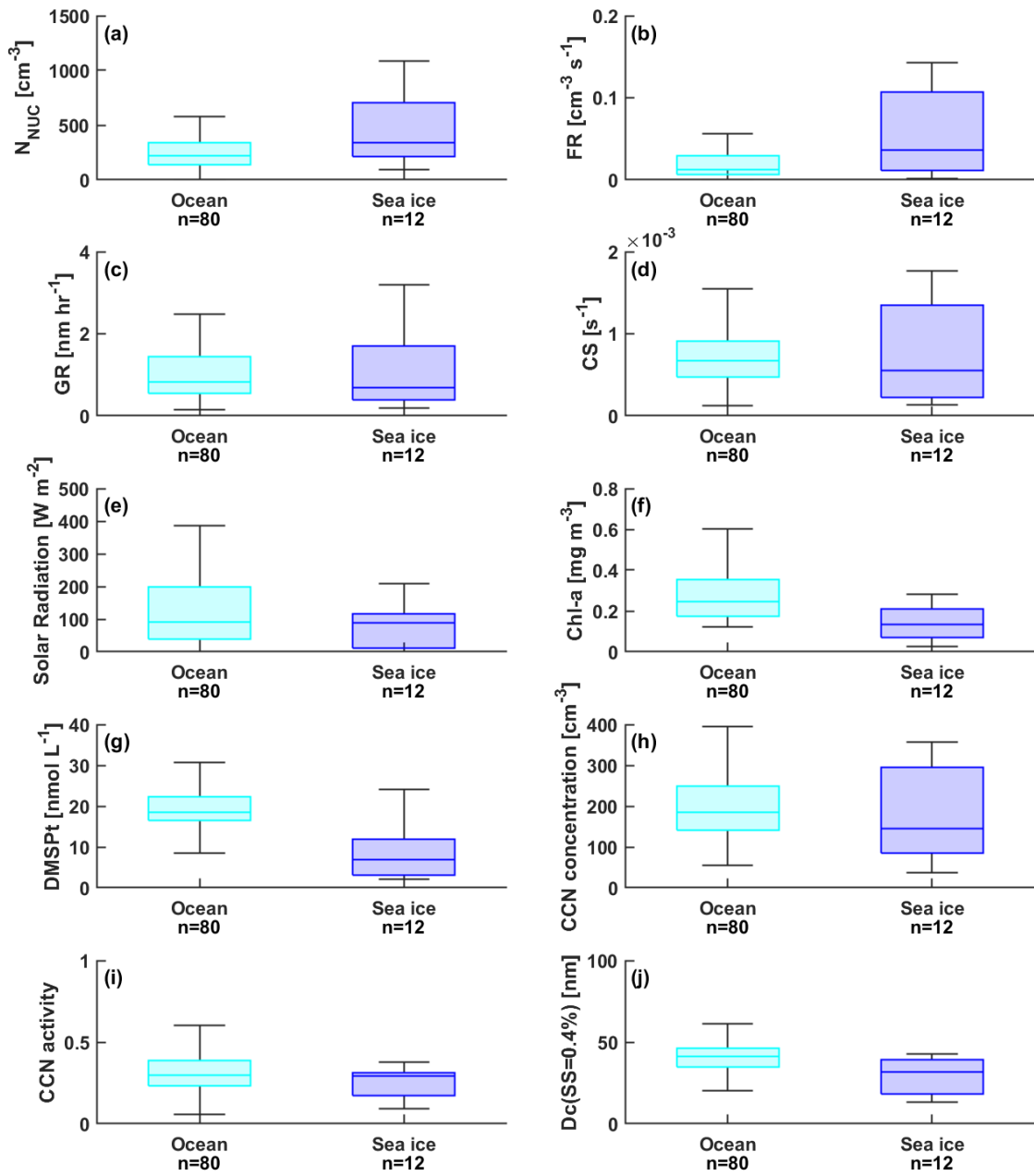


Figure 9. Box plots for (a) number concentration of nucleation-mode particles (N_{NUC}), (b) formation rate (FR), (c) growth rate (GR), (d) condensation sink (CS), (e) solar radiation, (f) chlorophyll exposure, (g) DMSP exposure, (h) CCN number concentration, (i) CCN activity, and (j) critical diameter (D_c) for ocean, sea ice, and multiple air masses. Upper/lower box limits and solid lines indicate the 75th/25th percentiles and median, respectively.

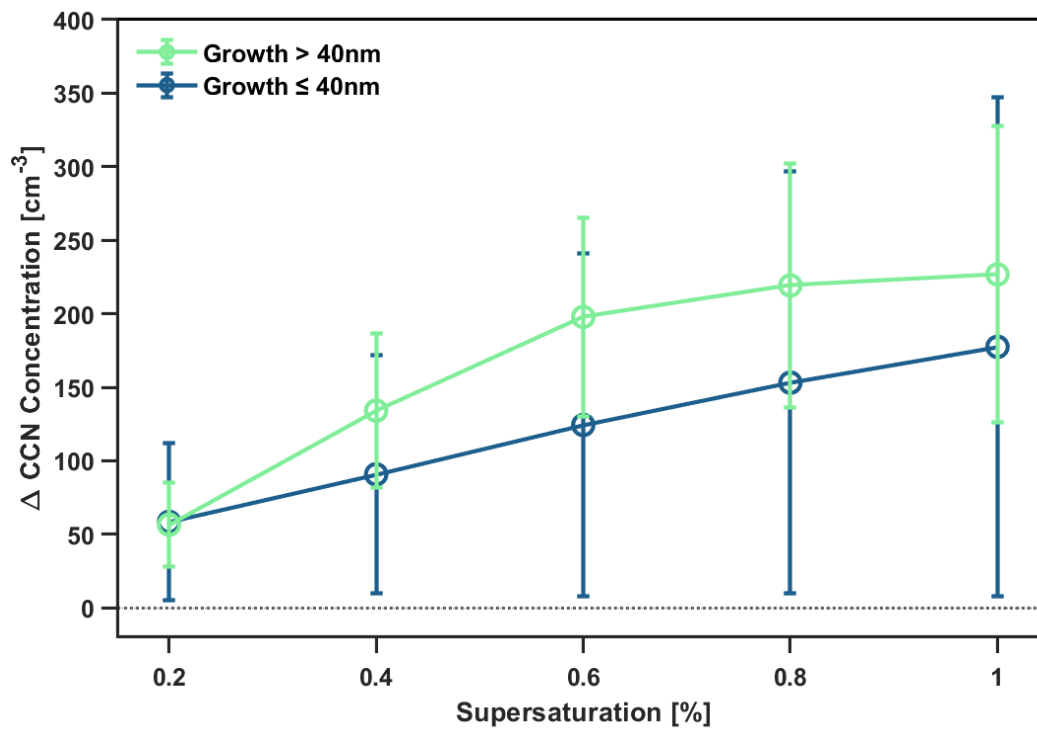


Figure 10. The increase in CCN concentration during growth to larger than 40 nm particles (green) and smaller than 40 nm (blue) times compared with background times at five different supersaturations.